Collective Solvent Coordinates for the Infrared Spectrum of HOD in D_2O Based on an ab Initio Electrostatic Map

Tomoyuki Hayashi, Thomas la Cour Jansen, Wei Zhuang, and Shaul Mukamel*

Department of Chemistry, University of California, Irvine, California 92697-2025

Received: July 26, 2004; In Final Form: September 23, 2004

An ab initio MP2 vibrational Hamiltonian of HOD in an external electrostatic potential parametrized by the electric field and its gradient-tensor is constructed. By combining it with the fluctuating electric field induced by the D_2O solvent obtained from molecular dynamics simulations, we calculate the infrared absorption of the O−H stretch. The resulting solvent shift and infrared line shape for three force fields (TIP4P, SPC/E, and SW) are in good agreement with the experiment. A collective coordinate response for the solvent effect is constructed by identifying the main electrostatic field and gradient components contributing to the line shape. This allows a realistic stochastic Liouville equation simulation of the line shapes which is not restricted to Gaussian frequency fluctuations.

I. Introduction

The structure and dynamic properties of liquid water have drawn considerable experimental and theoretical attention.[1−30] The structure was investigated using neutron[23] and X-ray scattering,[24] and reorientation was studied by NMR and dielectric relaxation experiments.[25] Water has strong intermolecular hydrogen bond interactions, which play an important role in a vast number of chemical and biological processes such as protein folding, protein−ligand binding, and DNA structure.

Ultrafast vibrational spectroscopy is a powerful tool for probing the structure and dynamics of condensed phase systems.[31−42] Vibrational frequencies of molecules in liquids are sensitive to the local environment. The frequency shift with respect to the gas phase provides information about the average liquid structure, whereas the line shapes reflect molecular dynamics. The vibrational properties of liquid water have received considerable attention.[7−22,31,43−45] Much experimental[9−17] and theoretical[18−21,43,44] effort has focused on the OH stretch of HOD in D_2O. This is a simpler system than neat water since that mode is spectrally isolated so that the rapid resonant intermolecular vibrational energy transfer[46] is eliminated.

Computing vibrational frequency fluctuations is the key for connecting the spectra with the details of the molecular structure and dynamics. In standard force fields,[47−50] electrostatic interactions are modeled using fixed atomic charges, and the electron density induced by response to the external potential is totally neglected. Polarizable force fields can overcome these limitations. One class of polarizable force fields utilize mobile charges to account for the polarizability.[51−54] A point charge is placed in a molecule and its position is adjusted to account for the dipole induced by the electrical fields. Alternatively, models with fluctuating point charges, where the charge on each atom is adjusted depending on the local electric field to mimic the polarizability, have been used.[55,56] Polarizable force fields based on the chemical potential equalization (CPE) principle[57,58] have been developed as well. Another type of polarizable force fields use continuous charge densities placed on different sites in the molecules instead of point charges.[56,59−62] A force field of this type was optimized to reproduce the vibrational frequencies of the water monomer.[62]

A number of approaches have been used to connect the spectra with the dynamics. In the first class, the vibrational frequencies are calculated using the same molecular dynamics (MD) force field used to describe the solvent, the solute, and the interaction between the two. To obtain the frequencies, the vibrational Hamiltonian is constructed and diagonalized at every time step. This is usually done by truncating the Hamiltonian at the harmonic level and diagonalizing the Hessian.[63,64] Classical MD potentials are designed mainly to reproduce intermolecular liquid structure, such as radial distribution functions, structure factor, diffusion constants, and dielectric constants. Therefore, classical force fields cannot be expected to give an accurate description of intramolecular vibrational potential energy surfaces.[65,66] A high level polarizable force field has been optimized to reproduce the vibrational frequencies of the water monomer.[62] This force field was applied to obtain the vibrational frequencies of static water clusters with up to six water molecules. The resulting solvent red shift of the OH stretch frequency was underestimated by up to 100 cm^{-1} for some cluster configurations.

The second class of simulations uses two force fields: A classical MD force field describes the solvent and solvent−solute interaction, while the solute vibrations are described by a different force field obtained from fit to experiment.[67,68] The vibrational Hamiltonian is again constructed for all time steps. To avoid repeated diagonalizations of the Hamiltonian, only the average Hamiltonian is diagonalized[67,69] and the instantaneous fluctuating Hamiltonians are transformed to the eigenbasis of the average Hamiltonian. Approximate fluctuating frequencies are obtained from the diagonal elements of the transformed Hamiltonians.[67,69] Alternatively, a perturbative approach is employed to avoid the time-consuming diagonalization.[43,70−74] In this approach, polarization effects can in principle be included

* To whom correspondence should be addressed.

10.1021/jp046685x CCC: $30.25
Published on Web 12/14/2004

by using a polarizable force field for the solvent and solvent−solute interaction.

The latest approach of this kind applied to HOD in D_2O[67,69] used a solute Hamiltonian fitted to experimental gas-phase data,[68] while the solute and solvent−solute interaction was accounted for using both the Lennard-Jones and electrostatic part of the TIP4P MD force field.[75] This approach gives −307 cm^{-1} for the OH stretch solvent shift, very close to the experiment (−312 cm^{-1}).[69] The line width was 64% of the experiment (163 vs 255 cm^{-1}). This approach requires detailed knowledge of the solute Hamiltonian from ab initio calculations or gas phase experiments. Even for a small molecule like water, it is computationally expensive to construct the Hamiltonian at numerous time steps along the trajectory and obtain the frequencies.

The third class of models use a MD force field for the solvent alone. The solvent−solute interaction and the solute are described by a map that accounts for the interaction only through the electrostatic field generated by the solvent force field.[13,44,76−79] The vibrational Stark effect, in which a uniform external field is applied and the effect on the vibrational spectrum is observed, has been applied to probe the local environment in proteins.[42,80,81] The map provides the frequencies as a function of the electrostatic potential[77−79] or its first derivative.[13,44,76] The simplest map utilized a quadratic Stark effect model based on a Morse potential for a single vibrational mode.[13] Other maps were based on fits to ab initio calculations on small clusters, establishing an empirical relation between the fundamental frequency and the electrostatic potential generated by a specific solvent force field.[44,77−79] These empirical maps provide a fast method for obtaining the fluctuating frequencies without constructing the full vibrational Hamiltonian at every time step. The solute polarization built into the ab initio maps is likely to be more important for the vibrational frequency than for the polarization of the solvent.

So far the only parameter used in the line shape simulations of HOD in D_2O was the electric field along the OH stretch direction.[13,44] The empirical ab initio maps reproduce the experimental solvent shift and line width.[44,77] Since the empirical relation is obtained from ab initio calculations of a specific solute−solvent cluster, it is not transferable and a new map needs to be constructed for different solvents and for each MD force field.[44] The computational cost for constructing the map grows rapidly with system size. Maps have been produced for the OH stretch of HOD in D_2O[44] and the amide I mode of an NMA−water cluster.[77−79] However, studying the effect of peptide−peptide interactions on the amide I mode requires much more expensive ab initio calculations of NMA in peptide residue clusters.

We present a new strategy for computing the trajectory of the vibrational frequency and apply it to the HOD/D_2O system based on an ab initio map of the solute frequencies as a function of the electric field and its gradient-tensor at some reference point obtained from a classical MD simulation. For each snapshot, we calculate the electric field and its derivatives at the reference point on the solute molecule using the same force field as in the simulation. The frequency is obtained from the map.

The Gaussian 03 code[82] only provides the energy gradient in a uniform electric field. Energy gradients are crucial for geometry optimizations and for calculating the anharmonic force constants. To construct the ab initio electrostatic map, we implemented the potential energy gradient calculation in the presence of an external nonuniform electric field to the Gaussian code.

Our approach has several advantages. First, the frequency shift fluctuations are given as the response of the solute to the entire profile of the local electrostatic potential. In contrast to existing empirical maps,[44,77] it includes both the electric field, and its gradient-tensor. Higher (second and third) order derivatives of the potential have been implemented, but were not necessary for the present application. Second, the present approach is not optimized to a particular solvent or force field and is therefore transferable. The map may be used to predict the fluctuating electrostatic environment and refine the force fields by optimizing the infrared spectra. Third, this approach provides a systematic way for identifying the relevant collective solvent coordinates which determine the frequency. This can be used to calculate the infrared spectra using the stochastic Liouville equation (SLE),[83−86] which is not limited to Gaussian frequency fluctuations. Finally, this ab initio map contains no empirical parameters.

Our main assumption is that the hydrogen bond effect on the OH stretch is purely electrostatic, independent of the covalent character of the hydrogen bonds. Other quantum effects such as exchange and electron transfer between solute and solvent are also neglected in our electrostatic map. The existence and importance of the covalent character of hydrogen bonds is a controversial issue. The covalent character of hydrogen bonds in ice and water were investigated by Compton X-ray scattering.[26] It has been recognized since Pauling[87] that the hydrogen bond in water is partially covalent. Much debate on this issue has followed, and several quantum chemical calculations have attempted to quantify the covalent contribution.[26,45,88,89] Recently, Isaacs and co-workers carried out an anisotropic X-ray Compton scattering experiment on ice.[26] Based on the fact that the Compton profile anisotropies calculated for superimposed water monomers did not exhibit the observed anisotropy, whereas calculations on ice using density-functional theory with a pseudo-potential and a plane wave basis do predict the observed periodic intensity oscillations in the Compton profile anisotropies as a function of momentum, they concluded that there is covalent bonding character in the hydrogen bonds in ice. A later calculation of the H_2O dimer by Davidson and coworkers[88] challenged this conclusion by showing that the same oscillations are already found when the unperturbed orbitals of the water monomers are used to construct a Slater determinant for the dimer, hence showing that the oscillations are irrelevant to the issue of the covalent character of the bond. By examining the electron density distribution along the O−H···O hydrogen bond, Parrinello et. al[45] showed that the wave functions in ice have a quantum-mechanical, multicenter character that gives rise to an antibonding, repulsive interaction between neighboring water molecules. (The charge density is reduced along the hydrogen bond coordinate compared with gas-phase water molecule.)

Our pure electrostatic model can reproduce the solvent shift and line width of the OH stretch quantitatively. This may be explained by comparing the electron density profiles of gas-phase water and ice along the O−H stretch direction made by Parrinello;[45] the two profiles are very close in the region of the covalent bonded O−H, and a small oscillation around the position of the other oxygen can be observed for ice and is absent for gas-phase water. This suggests that the covalent character of hydrogen bond does not have a very strong effect on the O−H stretch, as verified by our simulations.

In section II, we describe how the electric field is obtained from MD simulations for four force fields. The procedure for constructing the ab initio map for the frequencies is given in section III. (Details of the energy gradient calculation in an external nonuniform electric field are described in Appendix A.) The linear absorption calculated using the second-order cumulant expression by combining the MD simulations with the ab initio map are presented in section IV. A collective coordinate is identified in section V and the linear absorption is obtained using the SLE. The electrostatic components responsible for the infrared line shape are identified in section VI. A final discussion is given in section VII.

II. Electric Field Fluctuations

We have expanded the electrostatic potential U induced by the D_2O solvent to second order in the Cartesian components of the position X_α. ($\alpha,\beta = x, y, z$) around the center of charge of HOD

$$U(\mathbf{X}) = U_0 - \sum_\alpha E_\alpha X_\alpha - \frac{1}{2}\sum_\alpha\sum_\beta E_{\alpha\beta} X_\alpha X_\beta \qquad (1)$$

where the potential derivatives give the electric field components

$$E_\alpha = -\left(\frac{\partial U}{\partial X_\alpha}\right) \qquad (2)$$

and the second derivatives constitute the field gradient-tensor

$$E_{\alpha\beta} = -\left(\frac{\partial^2 U}{\partial X_\alpha \partial X_\beta}\right) \qquad (3)$$

Apart from U_0, eq 1 has nine independent parameters (note that $E_{\alpha\beta} = E_{\beta\alpha}$) arranged in a row vector $\mathbf{C}^\dagger = (E_x, E_y, E_z, E_{xx}, E_{yy}, E_{zz}, E_{xy}, E_{xz}, E_{yz})$. We used the coordinate system defined in Figure 1a. These parameters are obtained from the MD trajectories on rigid water molecules at each time step.

MD simulations were performed with four classical force fields. SPC/E[90] and TIP4P[75] are among the most popular force fields used for simulation of water and based on fixed point charges. SW[51] and SWM4[52] are polarizable. Both use one mobile charge adjusted to the local electric field to model the polarizability of the water molecule. The SW model was constructed to reproduce the gas-phase dipole, quadrupole, and dipole polarizability accurately.[51] The SWM4 model was only constrained to give the correct gas-phase dipole moment. The remaining parameters were optimized to reproduce bulk water properties such as vaporization enthalpy, density, static dielectric constant, and self-diffusion constant.[52]

SW and SWM4 only differ in the location of the mobile charge and the value of the parameters. The original models also differ in technical details of how the position of the charge is updated. In the original SW simulations[51] the set of equations for the many-body interactions between the particles was solved at each time step and the positions of the mobile charges were adjusted instantaneously. In the SWM4 simulations,[52] the mobile charge was assigned a small mass and short time steps were used allowing the mobile charge to respond almost instantaneously to the external field. In the present simulations, the equations that include the many-body interactions[51] are solved at each time step for both force fields.

All MD simulations were performed at a constant temperature 300 K and pressure 1 bar[91] with 1 fs time steps using the GROMACS package.[92] Simulation boxes with 215 D_2O and one HOD molecule were created for each of the four force fields. In all simulations the water molecules were kept rigid using the SHAKE algorithm.[93] A cutoff distance for both electrostatic and Lennard-Jones forces of 9 Å was used. Long-range electrostatic interactions were accounted for with the particle-mesh Ewald (PME) summation method.[94] The electric field and gradients were obtained from the trajectories at 4 fs time intervals. The trajectory lengths were 2.6 ns for the two nonpolarizable force fields (SPC/E and TIP4P) and 1.3 ns for the polarizable (SW and SWM4).

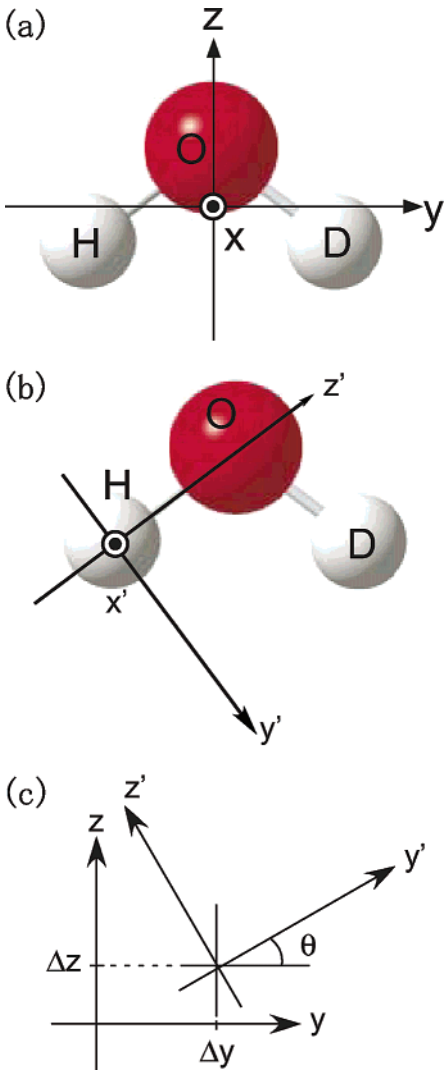

Figure 1. The coordinate system used in calculation of the anharmonic force field and the expansion of the electrostatic potential energy. (a) HOD is on the $y-z$ plane, and the x-axis is in perpendicular. The origin is at the center of charge. (b) The coordinate system fixed on the hydrogen atom used in the analysis of the contributions of the electrostatic components to the infrared line shape. z'-axis is parallel to the O−H bond. (c) Three parameters (Δy, Δz, and θ) which define the transformation between the two (Appendix C).

The electric field was calculated at the center of charge of HOD as

$$E_\alpha = \sum_{i,j} \frac{z_i r_{ji,\alpha}}{|r_{ji}|^3} \qquad (4)$$

z_i is the partial charge at solvent site i. $r_{ji,\alpha}$ is the αth Cartesian component of the distance vector between the center of charge on the solute j and the solvent site i. The center of charge is

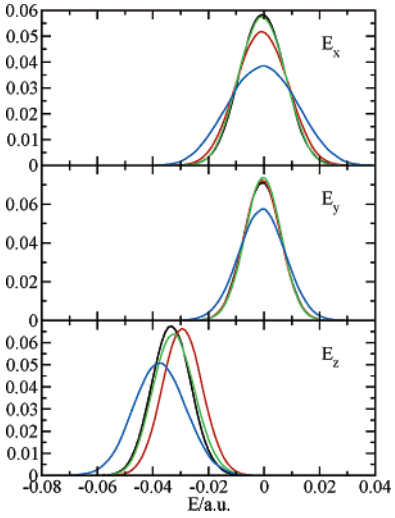

Figure 2. The distribution of the electric field Cartesian components. The colors indicate the different force fields. Black is SPC/E, red is TIP4P, green is SW, and blue is SWM4. The electric field is given in atomic units. (1 au = 51.422 V/Å)

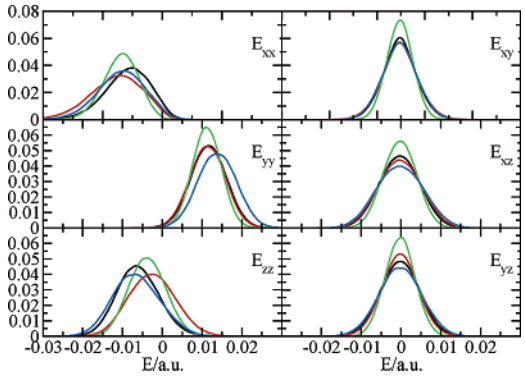

Figure 3. The distribution of the diagonal electric field gradients. The color is the same as in Figure 2. The electric field gradient is given in atomic units.

defined as $\boldsymbol{r}_{cc} = \sum_i Z_i \boldsymbol{r}_i / \sum_i Z_i$ where Z_i is the nuclear charge. The summation is truncated when the center of mass of the solvent and solute molecule exceeds 9 Å. These criteria ensure that all solvent charge sites are included keeping the system within the cutoff neutral. The electric field gradient tensor at the center of charge on the HOD molecule is

$$\frac{\partial E_\alpha}{\partial X_\beta} = \sum_{i,j} \frac{z_i(\delta_{\alpha\beta}|r_{ji}|^2 - 3r_{ji,\alpha}r_{ji,\beta})}{|r_{ji}|^5} \qquad (5)$$

The simulated electric field and gradient distributions are shown in Figures 2 and 3. For electric fields 1 au = 51.422 *V*/Å. For the gradients 1 au = 97.174 *V*/Å^2. The averages and variances of the electric fields and gradients are presented in Table 1 and 2. By symmetry $\langle E_x \rangle = \langle E_y \rangle = \langle E_{xy} \rangle = \langle E_{xz} \rangle = \langle E_{yz} \rangle = 0$. The non-zero average values of the field and gradients are the largest in SWM4, while the values for SW, TIP4P, and SPC/E are in general similar. The distribution of the fields is much broader for SWM4 than for the other force fields. The distribution of the gradients is narrowest for SW and broadest for SWM4. The *x* component distribution of the electric field is much broader than *y* and *z*. The *xx* gradient has a broader distribution than all other gradients. These broad distributions are connected with the out-of-plane direction. The fluctuating part of the electric field and gradients are denoted $\delta E(t) = E(t) - \langle E \rangle$. For all force fields, the covariances are small compared to the variances and only four components ($\langle \delta E_x \delta E_{xz} \rangle$, $\langle \delta E_z \delta E_{zz} \rangle$, $\langle \delta E_{xx} \delta E_{yy} \rangle$, and $\langle \delta E_{xx} \delta E_{zz} \rangle$) have a magnitude comparable to the variances as shown in Table 1 and 2.

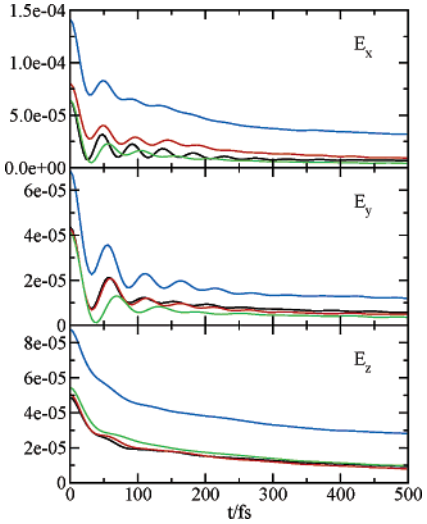

Figure 4. The autocorrelation functions of the electric field Cartesian components. The colors indicate the different force fields. The color is the same as in Figure 2.

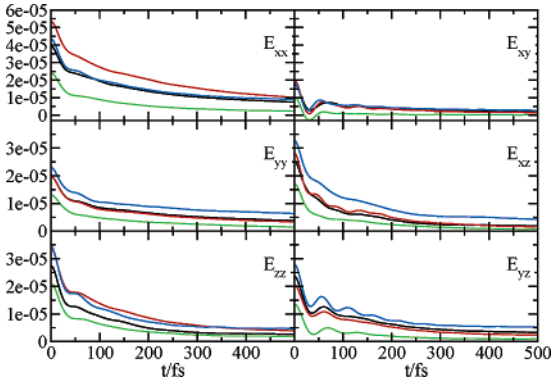

Figure 5. The autocorrelation functions of the electric field gradients. The color is the same as in Figure 2.

The electric field and gradient autocorrelation functions are displayed in Figures 4 and 5. These were fitted to a combination of two exponential functions and a damped oscillating function.

$$C(t) = A_1 \exp(-t/T_1) + A_2 \exp(-t/T_2) + A_3(\cos(\Omega t) + 1/(T_3\Omega)\sin(\Omega t))\exp(-t/T_3) \qquad (6)$$

The exponential functions corresponds to two strongly overdamped processes, and the oscillating term corresponds to a high-frequency underdamped Brownian oscillator in the high-temperature limit (eq 8.69 in ref 95). The fit parameters are given in Table 3 to 5. Some fits only required two terms. For other fits, the slowest exponential decay was too slow to allow an accurate determination of the decay constant from the correlation function with the given length. The exponential decay was then replaced by a constant by setting T_1 to ∞. All four force fields show similar general trends: E_x and E_y show damped oscillatory behavior. The oscillations are strongest for the *x* component, where the frequency of the oscillation is also higher. The damping is smallest for SPC/E and largest for SWM4. The frequencies are highest for SWM4 and lowest for SW. Along *z*, the correlation functions decay fast during the first 50 fs. At about 80 fs, there is a plateau and the correlation function then

TABLE 1: Ensemble Averages (in au), and Variance and Covariances (in 10^{-6} au^2) of the Each Electrostatic Component[a]

(a) TIP4P

		variance								
	average	δE_x	δE_y	δE_z	δE_{xx}	δE_{yy}	δE_{zz}	δE_{xy}	δE_{xz}	δE_{yz}
δE_x	−0.0001	76.4	0.3	0.3	−0.1	−0.2	−0.1	−0.1	−31.2	−0.1
δE_y	−0.0000	0.3	40.4	−0.1	0.3	−0.1	0.2	0.1	−0.2	−5.5
δE_z	−0.0284	0.3	−0.1	47.8	−3.9	−6.1	−12.2	0.0	−0.2	0.0
δE_{xx}	−0.0091	−0.1	0.3	−3.9	48.6	−14.8	23.3	0.0	0.1	0.1
δE_{yy}	0.0119	−0.2	−0.1	−6.1	−14.8	19.6	−4.5	0.1	0.0	0.0
δE_{zz}	0.0012	−0.1	0.2	−12.2	23.3	−4.5	33.4	−0.1	0.1	0.0
δE_{xy}	−0.0000	−0.1	0.1	0.0	0.0	0.1	−0.1	10.2	0.0	0.0
δE_{xz}	−0.0000	−31.2	−0.2	−0.2	0.1	0.0	0.1	0.0	33.5	0.0
δE_{yz}	−0.0000	−0.1	−5.5	0.0	0.1	0.0	0.0	0.0	0.0	5.8

(b) SPC/E

		variance								
	average	δE_x	δE_y	δE_z	δE_{xx}	δE_{yy}	δE_{zz}	δE_{xy}	δE_{xz}	δE_{yz}
δE_x	−0.0000	64.3	0.0	−0.3	−0.2	0.0	0.2	−0.3	21.5	−0.3
δE_y	−0.0000	0.0	43.7	−0.1	0.1	−0.1	0.0	0.1	−0.2	14.6
δE_z	−0.0327	−0.3	−0.1	48.8	−0.9	−11.9	12.8	−0.1	−0.4	−0.1
δE_{xx}	−0.0061	−0.2	0.1	−0.9	39.4	−15.8	−23.6	0.0	0.1	−0.1
δE_{yy}	0.0119	0.0	−0.1	−11.9	−15.8	19.7	−3.9	0.1	−0.1	0.1
δE_{zz}	−0.0058	0.2	0.0	12.8	−23.6	−3.9	27.5	0.0	0.0	0.0
δE_{xy}	−0.0000	−0.3	0.1	−0.1	0.0	0.1	0.0	17.8	0.0	0.1
δE_{xz}	−0.0001	21.5	−0.2	−0.4	0.1	−0.1	0.0	0.0	25.3	−0.2
δE_{yz}	0.0001	−0.3	14.6	−0.1	−0.1	0.1	0.0	0.1	−0.2	23.6

[a] The entry with the row δE_i and the column δE_j represents the covariance $\langle \delta E_i \delta E_j \rangle$. For electric fields 1 au = 51.422V/Å. For the gradients 1 au= 97.174V/Å^2.

TABLE 2: Ensemble Averages (in au), and Variance and Covariances (in 10^{-6} au^2) of the Each Electrostatic Component[a]

(c) SWM4

		δE_x	δE_y	δE_z	δE_{xx}	δE_{yy}	δE_{zz}	δE_{xy}	δE_{xz}	δE_{yz}
δE_x	0.0001	141.4	1.1	3.5	−1.2	−1.3	2.4	0.1	43.3	0.7
δE_y	−0.0001	1.1	68.7	0.3	0.3	−0.1	−0.2	0.0	0.1	21.3
δE_z	−0.0369	3.5	0.3	87.6	−7.3	−20.9	28.2	1.0	1.4	0.3
δE_{xx}	−0.0079	−1.2	0.3	−7.3	43.6	−16.0	−27.6	−0.3	0.3	0.6
δE_{yy}	0.0141	−1.3	−0.1	−20.9	−16.0	23.0	−7.0	−0.3	−1.1	−0.7
δE_{zz}	−0.0062	2.4	−0.2	28.2	−27.6	−7.0	34.5	0.6	0.7	0.2
δE_{xy}	−0.0000	0.1	0.0	1.0	−0.3	−0.3	0.6	18.8	0.4	−0.2
δE_{xz}	0.0001	43.3	0.1	1.4	0.3	−1.1	0.7	0.4	32.9	0.1
δE_{yz}	0.0001	0.7	21.3	0.3	0.6	−0.7	0.2	−0.2	0.1	28.0

(d) SW

		δE_x	δE_y	δE_z	δE_{xx}	δE_{yy}	δE_{zz}	δE_{xy}	δE_{xz}	δE_{yz}
δE_x	−0.0001	64.5	0.2	0.2	0.0	0.0	0.0	0.0	15.0	0.0
δE_y	0.0002	0.2	41.3	0.0	0.0	0.0	0.0	0.1	0.1	9.7
δE_z	−0.0317	0.2	0.0	54.5	−2.9	−8.5	11.4	0.1	0.0	−0.1
δE_{xx}	−0.0080	0.0	0.0	−2.9	24.2	−8.1	−16.0	0.0	0.1	−0.1
δE_{yy}	0.0115	0.0	0.0	−8.5	−8.1	13.1	−5.0	0.0	0.0	0.1
δE_{zz}	−0.0035	0.0	0.0	11.4	−16.0	−5.0	21.0	0.0	0.0	0.0
δE_{xy}	−0.0000	0.0	0.1	0.1	0.0	0.0	0.0	10.6	−0.1	−0.1
δE_{xz}	−0.0000	15.0	0.1	0.0	0.1	0.0	0.0	−0.1	17.1	0.0
δE_{yz}	−0.0000	0.0	9.7	−0.1	−0.1	0.1	0.0	−0.1	0.0	13.7

[a] The entry with the row δE_i and the column δE_j represents the covariance $\langle \delta E_i \delta E_j \rangle$. For electric fields 1 au = 51.422(V/Å). For the gradients 1 au = 97.174V/Å^2.

decays monotonically. The autocorrelation functions for the gradients are in general similar to that of the *z* component of the electric field, with the exception of *xy* and *yz* that show a damped oscillatory behavior.

III. The Ab Initio Electrostatic Map

A. Vibrational Hamiltonian and Eigenstates in an External Electrostatic Potential. Geometry optimization and the normal mode calculations of HOD in the gas phase were performed using Gaussian 03[82] at the MP2/6-31+G(d,p) level. The resulting anharmonic vibrational potential of HOD were expanded in the three normal coordinates (Q_1: mostly H−O−D bending, Q_2: mostly O−D stretch, and Q_3: mostly O−H stretch) will be denoted $V(\mathbf{Q};\mathbf{C}(t))$. V fluctuates with time, depending on the external electrostatic potential $U(\mathbf{X};\mathbf{C}(t))$ induced by the solvent. The potential energy of HOD in the electrostatic potential $U(\mathbf{X};\mathbf{C}(t))$ is expanded to sixth order in the three normal coordinates:

$$V(\mathbf{Q};\mathbf{C}) = \sum_i f_i^{(1)}(\mathbf{C})Q_i + \sum_{i,j} f_{ij}^{(2)}(\mathbf{C})Q_iQ_j + \sum_{i,j,k} f_{ijk}^{(3)}(\mathbf{C})Q_iQ_jQ_k + \sum_{i,j,k,l} f_{ijkl}^{(4)}(\mathbf{C})Q_iQ_jQ_kQ_l + \sum_{i,j,k,l,m} f_{ijklm}^{(5)}(\mathbf{C})Q_iQ_jQ_kQ_lQ_m + \sum_{i,j,k,l,m,n} f_{ijklmn}^{(6)}(\mathbf{C})Q_iQ_jQ_kQ_lQ_mQ_n \quad (7)$$

TABLE 3: Parameters for the Electric Field Correlation Function Fit to Eq 6 for SPC/E, TIP4P, SW, and SWM4[a]

	E_x				E_y				E_z			
	SPC/E	TIP4P	SW	SWM4	SPC/E	TIP4P	SW	SWM4	SPC/E	TIP4P	SW	SWM4
A_1	18.5	33.7	21.6	31.0	10.2	7.62	7.62	19.1	21.8	23.7	24.2	46.8
T_1	410	351	240	∞	843	1021	618	993	569	446	531	911
A_2	24.4	33.9	0.0	66.7	13.9	15.7	10.6	33.8	28.4	24.2	19.4	43.1
T_2	24.5	21.6	0.0	140.7	65.9	83.5	43.8	44.5	31.2	35.9	60.7	39.8
A_3	24.3	17.5	45.3	47.1	21.2	21.2	24.7	18.6	1.21	4.72	12.0	0.0
Ω	0.134	0.126	0.105	0.115	0.106	0.104	0.088	0.111	0.105	0.094	0.066	0.0
T_3	67.8	60.9	24.7	23.4	41.9	44.2	39.0	65.6	60.0	40.5	23.3	0.0

[a] The amplitudes A_1, A_2, and A_3 are given in units of 10^{-6} au. T are in fs and Ω in fs^{-1}.

TABLE 4: Parameters for the Electric Field Gradient Correlation Function Fit to Eq 6 for TIP4P and SPC/E[a]

	E_{xx}		E_{yy}		E_{zz}		E_{xy}		E_{xz}		E_{yz}	
	TIP4P	SPC/E	TIP4P	SPC/E	TIP4P	SPC/E	TIP4P	SPC/E	TIP4P	SPC/E	TIP4P	SPC/E
A_1	15.3	10.7	9.19	8.40	3.27	2.40	0.0	0.0	12.3	8.95	1.72	2.73
T_1	906	1207	469	608	∞	∞	0.0	0.0	218	260	∞	∞
A_2	25.4	20.5	9.61	6.39	21.6	16.9	7.19	7.12	14.1	17.3	12.5	13.5
T_2	171	133	38.1	73.2	142	108	278	357	26.6	31.5	158	149
A_3	13.5	8.71	1.65	5.32	9.44	8.69	13.2	10.7	3.39	0.0	6.73	7.92
Ω	0.039	0.082	0.091	0.069	0.085	0.088	0.102	0.093	0.121	0.0	0.092	0.094
T_3	11.1	18.6	40.5	15.3	21.2	19.8	33.0	32.7	31.5	0.0	31.2	33.1

[a] The amplitudes A_1, A_2, and A_3 are given in units of 10^{-6} au. T are in fs and Ω in fs^{-1}.

TABLE 5: Parameters for the Electric Field Correlation Function Fit to Eq 6 for SWM4 and SW[a]

	E_{xx}		E_{yy}		E_{zz}		E_{xy}		E_{xz}		E_{yz}	
	SWM4	SW	SWM4	SW	SWM4	SW	SWM4	SW	SWM4	SW	SWM4	SW
A_1	11.2	3.69	11.0	5.21	4.55	1.78	2.01	0.0	13.1	6.30	4.85	0.75
T_1	1834	925	881	393	∞	∞	∞	0.0	386	205	∞	∞
A_2	21.9	13.0	11.6	3.89	22.1	11.9	6.11	1.11	19.6	12.3	15.7	6.00
T_2	123	118	40.3	61.9	94	105	199	281	41.1	19.2	120	127
A_3	11.2	7.83	1.18	4.25	8.67	7.70	10.8	9.78	0.0	0.0	8.13	7.28
Ω	0.080	0.073	0.103	0.057	0.096	0.076	0.114	0.102	0.0	0.0	0.107	0.085
T_3	15.3	21.3	56.4	18.5	22.2	22.4	30.2	29.3	0.0	0.0	41.0	33.3

[a] The amplitudes A_1, A_2, and A_3 are given in units of 10^{-6} au. T are in fs and Ω in fs^{-1}.

where

$$f^{(n)}_{l_1\cdots l_n} \equiv \frac{1}{n!}\left(\frac{\partial^n V}{\partial Q_{l_1}\cdots\partial Q_{l_n}}\right) \tag{8}$$

We implemented the potential energy gradient calculation in the presence of nonuniform external electric field to the Gaussian 03 program (Appendix A).

The harmonic and anharmonic (third, fourth, fifth, and sixth) force constants were calculated by numerical derivatives of the first analytical derivative of the potential energy obtained by using the modified Gaussian 03 program at the same level as the gas-phase calulcation. The procedure is described in Appendix B. The resulting expansion coefficients in eq 7 for $\mathbf{C} = \mathbf{0}$ are tabulated in Supporting Information.

The vibrational eigenstates in the electrostatic potential $U(\mathbf{X};\mathbf{C})$ were expanded in a Hartree product basis of harmonic oscillator eigenfunctions.

$$|\psi_a(\mathbf{C})\rangle = \sum_{n_1,n_2,n_3} |n_1, n_2, n_3\rangle\langle n_1, n_2, n_3|\psi_a(\mathbf{C})\rangle \tag{9}$$

where $|n_1, n_2, n_3\rangle \equiv |n_1\rangle|n_2\rangle|n_3\rangle$, and $|n_i\rangle$ represents the nth eigenfunction of the harmonic potential of coordinate i. The Hamiltonian was recast into a normal ordered form[96] where the coordinates Q_i and momenta P_i are expressed by bosonic creation ($B_i^\dagger$) and annihilation (B_i) operators:

$$Q_i = \sqrt{\frac{\hbar}{2m_i\omega_i}}(B_i^\dagger + B_i) \tag{10}$$

$$P_i = i\sqrt{\frac{m_i\hbar\omega_i}{2}}(B_i^\dagger - B_i) \tag{11}$$

where m_i and ω_i are the effective mass and the frequency of each harmonic mode i, respectively. The vibrational eigenstates are obtained by diagonalizing the Hamiltonian using the implicit restarted Arnoldi method (IRAM).[96−98] High energy basis states where the total number of excitations $n_T \equiv n_1 + n_2 + n_3$ are larger than 14 are neglected. The total number of states is 452. We checked the convergence of the frequencies varying the size of the basis set (n_T), and all the states reported in Table 6 are converged within 1 cm^{-1} at $n_T = 14$. The dependence of the eigenstate frequencies on the n_T is displayed in Supporting Information.

The gas-phase calculated vibrational eigenstates ($\mathbf{C} = 0$) are shown in Table 6 together with their IR intensities and eigenvectors. The simulated O−H stretch fundamental 3756 cm^{-1} (state 5) agrees within 1.3% with the experiment (3707 cm^{-1}).[99] This accuracy is reasonable at the ab initio (MP2/6-31+G(d,p)) level. State 17 (7359 cm^{-1}) is the first overtone of the O−H stretch vibration. The O−H stretch anharmonicity $\Delta\omega \equiv 2\omega_5 - \omega_{17}$ (153 cm^{-1}) agrees with an earlier calculation that

TABLE 6: Calculated Vibrational Eigenstates of HOD in the Gas Phase[a]

state	frequency		intensity	description	eigenvector				
1		0.0	−	GS	−0.99(000)	−0.10(010)			
2		1385.2	142.06	δ(H−O−D)	−0.99(100)				
3	(2782)	2739.8	2.53	δ(H−O−D)$_{v=2}$	+0.39(010)	−0.90(200)	+0.11(020)		
4	(2724)	2778.9	31.22	ν(O−D)	+0.86(010)	+0.40(200)	+0.25(020)		
5	(3707)	3756.3	73.34	ν(O−H)	+0.93(001)	+0.11(200)	+0.27(002)	+0.12(011)	
6	(4146)	4076.4	0.01	δ(H−O−D)$_{v=3}$	+0.26(110)	+0.18(101)	−0.92(300)	−0.12(400)	
7	(4100)	4174.0	0.37		+0.91(110)	+0.26(300)	+0.26(120)		
8	(5090)	5104.6	0.14		−0.94(101)	−0.18(300)	−0.22(102)	−0.11(111)	
9		5391.6	0.00		−0.15(300)	−0.23(210)	−0.24(201)	+0.88(400)	+0.17(500)
10	(5364)	5460.9	0.37	ν(O−D)$_{v=2}$	+0.27(010)	−0.80(020)	−0.44(030)	+0.18(210)	−0.14(040)
11		5549.5	0.02		+0.16(020)	−0.10(011)	+0.90(210)	+0.21(400)	+0.25(220)
12	(6452)	6431.4	0.01		−0.13(002)	−0.16(011)	+0.91(201)	+0.25(400)	+0.15(202)
13	(6416)	6518.1	0.03		−0.12(001)	+0.87(011)	+0.24(012)	+0.17(201)	+0.28(021)
14		6693.2	0.00		+0.25(400)	+0.21(310)	+0.29(301)	−0.82(500)	−0.22(600)
15		6848.0	0.00		−0.22(110)	+0.69(120)	+0.37(130)	−0.50(310)	−0.14(500)
16		6913.7	0.00		+0.16(110)	−0.45(120)	−0.25(130)	−0.75(310)	−0.21(320)
17		7359.2	0.83	ν(O−H)$_{v=2}$	+0.28(001)	−0.78(002)	−0.46(003)	−0.16(004)	−0.13(005)
18		7730.8	0.00		−0.24(102)	−0.17(111)	+0.86(301)	+0.32(500)	

[a] The frequencies are given in cm^{-1} and the infrared intensities are in 10^4 D^2 Bohr^{-2}. The frequencies in parentheses are the frequency from experiment.[99] ($n_1n_2n_3$) represents the state where there are n_1, n_2, and n_3 vibrational quanta for mode 1, 2, and 3.

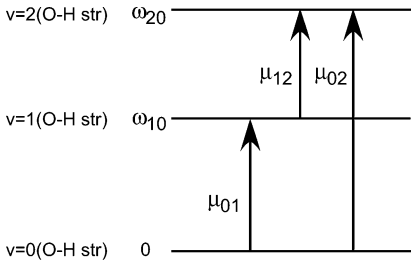

Figure 6. Energy level diagram for the OH stretch in HOD. The model has five vibrational parameters (two transition frequencies and three transition dipole moments) relevant for the infrared spectra.

used a potential energy surface fitted to reproduce the gas-phase vibrational spectra of H_2O (163 cm^{-1}).[18]

B. Parametrization of the Vibrations. Molecular vibrational eigenstates and transition dipole moments were parametrized with the electrostatic components **C**. The resulting ab initio electrostatic map can be used for a low-cost calculation of the transition frequencies and transition dipole moments at each time step of a MD trajectory, avoiding repeated ab initio calculations.

We focus on the O−H stretch mode and consider the ground state (g), the fundamental (e), and the O−H stretch first overtone (f). The vibrational quantities related to this 3 level system are two transition frequencies ($g \rightarrow e$ and $g \rightarrow f$) and three transition dipole moments ($g \rightarrow e$, $g \rightarrow f$, and $e \rightarrow f$) (see Figure 6). An ab initio map was constructed for these five quantities. The ab initio map frequencies ω_{am} and transition dipoles $\mu_\alpha(\alpha = x, y, z)$ were expanded to quadratic order in **C**:

$$\omega_{am} = \omega^{gas} + \Omega^{(1)\dagger}\mathbf{C} + \frac{1}{2}\mathbf{C}^\dagger\Omega^{(2)}\mathbf{C} \quad (12)$$

$$\mu_\alpha = \mu_\alpha^{gas} + \mathbf{M}_\alpha^{(1)\dagger}\mathbf{C} + \frac{1}{2}\mathbf{C}^\dagger\mathbf{M}_\alpha^{(2)}\mathbf{C} \quad (\alpha = x, y, z) \quad (13)$$

where $\Omega^{(1)}$ is a nine-component row vector and $\Omega^{(2)}$ is a 9×9 matrix defined as

$$\Omega^{(1)^\dagger} \equiv \left(\frac{\partial\omega}{\partial E_x}, \ldots, \frac{\partial\omega}{\partial E_{yz}}\right) \quad (14)$$

$$(\Omega^{(2)})_{ij} \equiv \left(\frac{\partial^2\omega}{\partial E_i \partial E_j}\right) \quad (15)$$

$\mathbf{M}^{(1)}$ and $\mathbf{M}^{(2)}$ are defined in the same way. Equation 12 is the ab initio electrostatic map for the transition frequencies, and eq 13 is the ab initio electrostatic map for the transition dipole moments.

Expanding the O−H stretch fundamental frequency ω around the average electrostatic fields $\langle\mathbf{C}\rangle$; eq 12 is transformed to

$$\omega_{am} = \omega_{eq} + \Omega_{eq}^{(1)\dagger}\delta\mathbf{C} + \frac{1}{2}\delta\mathbf{C}^\dagger\Omega_{eq}^{(2)}\delta\mathbf{C} \quad (16)$$

where $\delta\mathbf{C} \equiv \mathbf{C} - \langle\mathbf{C}\rangle$, and ω_{eq}, $\Omega_{eq}^{(1)}$ and $\Omega_{eq}^{(2)}$ are connected to the expansion coefficients in eq 12 as

$$\omega_{eq} = \omega^{gas} + \Omega^{(1)\dagger}\langle\mathbf{C}\rangle + \frac{1}{2}\langle\mathbf{C}^\dagger\rangle\Omega^{(2)}\langle\mathbf{C}\rangle \quad (17)$$

$$\Omega_{eq}^{(1)} = \Omega^{(1)} + \Omega^{(2)\dagger}\langle\mathbf{C}\rangle \quad (18)$$

$$\Omega_{eq}^{(2)} = \Omega^{(2)} \quad (19)$$

$\Omega_{eq}^{(1)}$ is the vector ($\omega_x^{(1)}$, $\omega_y^{(1)}$, $\omega_z^{(1)}$, $\omega_{xx}^{(1)}$, $\omega_{yy}^{(1)}$, $\omega_{zz}^{(1)}$, $\omega_{xy}^{(1)}$, $\omega_{xz}^{(1)}$, $\omega_{yz}^{(1)}$).

The resulting parameters for the transition frequencies and transition dipoles are shown in Tables 7 and 8 respectively. $\Omega_{eq}^{(1)}$ and $\langle\mathbf{C}\rangle$ are given in Table 11.

IV. Frequency Trajectory and the Linear Infrared Absorption

Trajectories of the frequencies and transition dipole moments were calculated using eqs 12 and 13 and the electrostatic components $\mathbf{C}(t)$ for the four force fields. We used the experimental value 3707 cm^{-1} for the O−H stretch fundamental gas-phase frequency ω^{gas} in eq 12 rather than the ab initio (3756 cm^{-1}) value.

The static distribution of the simulated O−H stretch fundamental are displayed in Figure 7. The distributions are asymmetric and have a longer tail to the red. Since most of the electrostatic components have symmetric Gaussian static distributions, this deviation primarily comes from the quadratic relation between the frequency and the electrostatic components (eq 12). The SW force field has the narrowest distribution, TIP4P and SPC/E are very similar, and SWM4 is much broader and red shifted compared to the other force fields.

TABLE 7: Ab Initio Electrostatic Map of O−H Stretch Transition Frequencies (ω_{ge} and ω_{gf}) (eq 12)[a]

parameter	calculation	parameter	calculation
ω_{ge}^{gas}	3756.3	ω_{gf}^{gas}	7359.2
$\omega_{ge\,x}^{(1)}$	0	$\omega_{gf\,x}^{(1)}$	0
$\omega_{ge\,y}^{(1)}$	1449	$\omega_{gf\,y}^{(1)}$	2826
$\omega_{ge\,z}^{(1)}$	1732	$\omega_{gf\,z}^{(1)}$	3358
$\omega_{ge\,xx}^{(1)}$	6596	$\omega_{gf\,xx}^{(1)}$	13150
$\omega_{ge\,yy}^{(1)}$	−2398	$\omega_{gf\,yy}^{(1)}$	−5130
$\omega_{ge\,zz}^{(1)}$	−4280	$\omega_{gf\,zz}^{(1)}$	−8783
$\omega_{ge\,yz}^{(1)}$	−8886	$\omega_{gf\,yz}^{(1)}$	−17977
$\omega_{ge\,x,x}^{(2)}$	−9778	$\omega_{gf\,x,x}^{(2)}$	−17832
$\omega_{ge\,y,y}^{(2)}$	−86288	$\omega_{gf\,y,y}^{(2)}$	−174611
$\omega_{ge\,y,z}^{(2)}$	−92644	$\omega_{gf\,y,z}^{(2)}$	−196521
$\omega_{ge\,y,yy}^{(2)}$	422939	$\omega_{gf\,y,yy}^{(2)}$	853883
$\omega_{ge\,y,zz}^{(2)}$	18782	$\omega_{gf\,y,zz}^{(2)}$	69115
$\omega_{ge\,y,yz}^{(2)}$	239319	$\omega_{gf\,y,yz}^{(2)}$	487109
$\omega_{ge\,z,z}^{(2)}$	−50713	$\omega_{gf\,z,z}^{(2)}$	−104064
$\omega_{ge\,z,yy}^{(2)}$	126072	$\omega_{gf\,z,yy}^{(2)}$	303398
$\omega_{ge\,z,zz}^{(2)}$	159186	$\omega_{gf\,z,zz}^{(2)}$	323845
$\omega_{ge\,z,yz}^{(2)}$	147880	$\omega_{gf\,z,yz}^{(2)}$	303551
$\omega_{ge\,xx,xx}^{(2)}$	−101703	$\omega_{gf\,xx,xx}^{(2)}$	−206247
$\omega_{ge\,yy,yy}^{(2)}$	−832909	$\omega_{gf\,yy,yy}^{(2)}$	−1689434
$\omega_{ge\,yy,zz}^{(2)}$	410669	$\omega_{gf\,yy,zz}^{(2)}$	765958
$\omega_{ge\,yy,yz}^{(2)}$	−407944	$\omega_{gf\,yy,yz}^{(2)}$	−893856
$\omega_{ge\,zz,zz}^{(2)}$	−296671	$\omega_{gf\,zz,zz}^{(2)}$	−589828
$\omega_{ge\,zz,yz}^{(2)}$	−182787	$\omega_{gf\,zz,yz}^{(2)}$	−368953
$\omega_{ge\,xy,xy}^{(2)}$	−27790	$\omega_{gf\,xy,xy}^{(2)}$	−57224
$\omega_{ge\,xz,xz}^{(2)}$	−21258	$\omega_{gf\,xz,xz}^{(2)}$	−41630
$\omega_{ge\,yz,yz}^{(2)}$	−192522	$\omega_{gf\,yz,yz}^{(2)}$	−398205

[a] Parameters equal to zero are omitted. The first derivatives of the frequencies are given in units of cm^{-1} au^{-1}, and the second derivatives are in units of cm^{-1} au^{-2}.

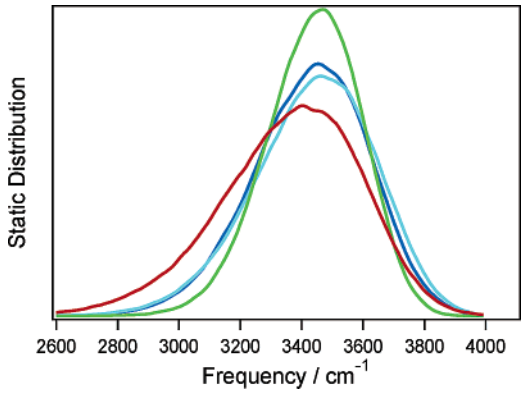

Figure 7. Static distribution of the O−H stretch fundamental frequency using the ab initio map for four different force fields used in the MD simulation and the calculation of the electrostatic potential. Blue: TIP4P; skyblue: SPC/E; red: SWM4; green: SW. A black vertical arrow represents the gas-phase frequency.[99]

The static distributions of the transition dipole moment $|\mu_{ge}|$ for the four force fields are given in Figure 8. TIP4P, SPC/E, and SW have similar amplitudes (∼20 D $Bohr^{-1}$) that are much larger than the gas-phase value (8.56 D $Bohr^{-1}$) due to the polarization induced by the solvation and the hydrogen bonding. SWM4 has a larger amplitude (23 D $Bohr^{-1}$) and a broader distribution compared to the other force fields. The time

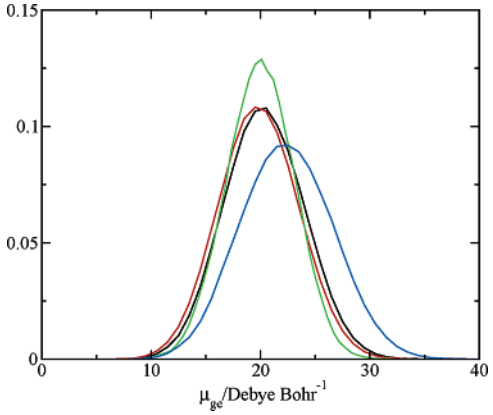

Figure 8. The distribution of the transition dipole moment μ_{ge} for the four force fields. The colors are the same as in Figure 2.

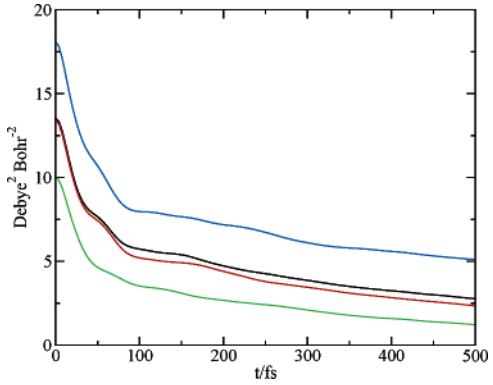

Figure 9. Correlation functions of the transition dipole moment μ_{ge} for the four force fields. Color codes are the same as in Figure 2.

correlation functions for the fluctuating part of the transition dipoles $|\mu_{ge}|$ are given in Figure 9. The fluctuations are much smaller than the average dipole moments. The variance of the fluctuations are 10−16 D^2 $Bohr^{-2}$ compared to the square of the average dipole of 361−576 D^2 $Bohr^{-2}$. These fluctuations can safely be neglected when calculating the response function.

The linear response was calculated using the cumulant expansion of Gaussian fluctuations (CGF).[100,101]

$$S^{(1)}(t_1) = i\theta(t_1)[J(t_1) - J^*(t_1)] \tag{20}$$

$J(t_1) = \langle\mu(t_1)\mu(0)\rangle$ is a two time correlation function of the transition dipole μ. In the Condon approximation, where the transition dipole operator is independent of the bath coordinates we have

$$J(t_1) = \sum_{ij}|\mu_{ij}|^2\exp[-i\langle\omega_{ij}\rangle t_1 - g_{ij}(t_1)] \tag{21}$$

where $\langle\omega_{ij}\rangle$ is the average transition frequency and $g_{ij}(t_1)$ is the line-broadening function for the transition between state i and j. μ_{ij} is the transition dipole between the states i and j. The line-broadening function is related to the correlation function of the transition frequency.

$$g_{ij}(t) = \int_0^t d\tau_2 \int_0^{\tau_2} d\tau_1 C_{ij}(\tau_1) \tag{22}$$

where $C_{ij}(t)$ are the ground-state quantum correlation functions of the frequency:

$$C_{ij}(\tau_1) \equiv \langle\delta\omega_{ij}(\tau_1)\delta\omega_{ij}(0)\rangle \tag{23}$$

TABLE 8: Ab Initio Electrostatic Map of O−H Stretch Transition Dipole Moment ($g \rightarrow e$, $g \rightarrow f$, and $e \rightarrow f$) (eq 13)[a]

parameter	calculation	parameter	calculation	parameter	calculation
μ_{ge}^{gas}	(0, 8.02, 2.99)	μ_{gf}^{gas}	(0, 0.84, 0.36)	μ_{ef}^{gas}	(0, 11.50, 4.30)
$\mu_{ge\,x}^{(1)}$	(−40, 0, 0)	$\mu_{gf\,x}^{(1)}$	(−5, 0, 0)	$\mu_{ef\,x}^{(1)}$	(−57, 0, 0)
$\mu_{ge\,y}^{(1)}$	(0, −198, −137)	$\mu_{gf\,y}^{(1)}$	(0, −22, −14)	$\mu_{ef\,y}^{(1)}$	(0, −281, −197)
$\mu_{ge\,z}^{(1)}$	(0, −108, −119)	$\mu_{gf\,z}^{(1)}$	(0, −12, −13)	$\mu_{ef\,z}^{(1)}$	(0, −154, −170)
$\mu_{ge\,xx}^{(1)}$	(0, −49, −12)	$\mu_{gf\,xx}^{(1)}$	(0, −6, −2)	$\mu_{ef\,xx}^{(1)}$	(0, −71, −17)
$\mu_{ge\,yy}^{(1)}$	(0, 461, 224)	$\mu_{gf\,yy}^{(1)}$	(0, 50, 25)	$\mu_{ef\,yy}^{(1)}$	(0, 666, 313)
$\mu_{ge\,zz}^{(1)}$	(0, −15, 92)	$\mu_{gf\,zz}^{(1)}$	(0, −87, −37)	$\mu_{ef\,zz}^{(1)}$	(0, −1193, −443)
$\mu_{ge\,xy}^{(1)}$	(−4, 0, 0)	$\mu_{gf\,xy}^{(1)}$	(0, 0, 0)	$\mu_{ef\,xy}^{(1)}$	(−6, 0, 0)
$\mu_{ge\,xz}^{(1)}$	(9, 0, 0)	$\mu_{gf\,xz}^{(1)}$	(1, 0, 0)	$\mu_{ef\,xz}^{(1)}$	(13, 0, 0)
$\mu_{ge\,yz}^{(1)}$	(0, 233, 164)	$\mu_{gf\,yz}^{(1)}$	(0, 27, 18)	$\mu_{ef\,yz}^{(1)}$	(0, 331, 234)
$\mu_{ge\,x,x}^{(2)}$	(0, 416, 178)	$\mu_{gf\,x,x}^{(2)}$	(0, 42, 22)	$\mu_{ef\,x,x}^{(2)}$	(0, 602, 242)
$\mu_{ge\,y,y}^{(2)}$	(0, −408, −529)	$\mu_{gf\,y,y}^{(2)}$	(0, −13, −54)	$\mu_{ef\,y,y}^{(2)}$	(0, −599, −748)
$\mu_{ge\,z,z}^{(2)}$	(0, 136, 364)	$\mu_{gf\,z,z}^{(2)}$	(0, 31, 46)	$\mu_{ef\,z,z}^{(2)}$	(0, 167, 556)
$\mu_{ge\,xx,xx}^{(2)}$	(0, 2568, 1253)	$\mu_{gf\,xx,xx}^{(2)}$	(0, 290, 153)	$\mu_{ef\,xx,xx}^{(2)}$	(0, 3712, 1763)
$\mu_{ge\,yy,yy}^{(2)}$	(0, 4226, −3089)	$\mu_{gf\,yy,yy}^{(2)}$	(0, 679, −235)	$\mu_{ef\,yy,yy}^{(2)}$	(0, 6312, −4882)
$\mu_{ge\,zz,zz}^{(2)}$	(0, 6100, 1860)	$\mu_{gf\,zz,zz}^{(2)}$	(0, −16675, −9375)	$\mu_{ef\,zz,zz}^{(2)}$	(0, −225131, −112986)
$\mu_{ge\,xy,xy}^{(2)}$	(0, 716, 530)	$\mu_{gf\,xy,xy}^{(2)}$	(0, 78, 64)	$\mu_{ef\,xy,xy}^{(2)}$	(0, 1044, 740)
$\mu_{ge\,xz,xz}^{(2)}$	(0, 628, 492)	$\mu_{gf\,xz,xz}^{(2)}$	(0, 64, 60)	$\mu_{ef\,xz,xz}^{(2)}$	(0, 914, 684)
$\mu_{ge\,yz,yz}^{(2)}$	(0, −1536, −1193)	$\mu_{gf\,yz,yz}^{(2)}$	(0, −41, −69)	$\mu_{ef\,yz,yz}^{(2)}$	(0, −2323, −1777)

[a] Columns in parentheses represent (x,y,z) components. The transition dipole moments are in 10^2 D Bohr^{-1}. The first derivatives are given in units of 10^2 D Bohr^{-1} au^{-1}, and the second derivatives are in 10^2 D Bohr^{-1} au^{-2}.

$\delta\omega(t) \equiv \omega(t) - \langle\omega\rangle$ and $C_{ij}(t)$ is calculated using the Wiener-Khinchin relation[47] with the harmonic quantum correction.[95] The quantum correlation function in the frequency domain is related to its classical counterpart as

$$\tilde{C}_{ij}(f) = \frac{\hbar f}{2k_B T}\left(\coth\left(\frac{\hbar f}{2k_B T}\right) + 1\right)|\tilde{\delta\omega}_{ij}(f)|^2 \qquad (24)$$

where

$$\tilde{A}(f) \equiv \int_{-\infty}^{\infty} dt\, \exp(ift)A(t) \qquad (25)$$

The vibrational Stokes shift is given by the slope of the imaginary part of the line broadening function $g_{ij}(t)$ as time goes to infinity.[95] We have calculated the Stokes shift for the O−H stretch fundamental by fitting the imaginary part of $g_{ge}(t)$ between 4 and 6 ps to a straight line.

The correlation functions of the fundamental frequencies for the four force fields are shown in Figure 10. All force fields show small bumps on the shoulder of the decay profiles in agreement with earlier simulations.[13,43,67,69] The feature is slightly less pronounced compared to these earlier works, but comparable to that obtained from the empirical map.[44] The real part of the correlation functions was fitted to

$$C(t) = A_1 \exp(-t/T_1) + A_2 \exp(-t/T_2) + A_3(\cos(\Omega t)) + 1/(\Omega T_3)\sin(\Omega t))\exp(-t/T_3) + A_4(\cos(\Omega' t)) + 1/(\Omega' T_4)\sin(\Omega t))\exp(-t/T_4) \qquad (26)$$

The fit parameters are given in Table 9. The exponential decay time for SWM4 is much slower than for the other force fields. SW does not show any oscillations. One of the oscillations is replaced with an exponential decay for this force field (the frequency of the oscillation is zero). The other oscillatory term was set to zero in the fit. SPC/E, SWM4, and TIP4P could not be fitted well using only one oscillatory term. The frequencies

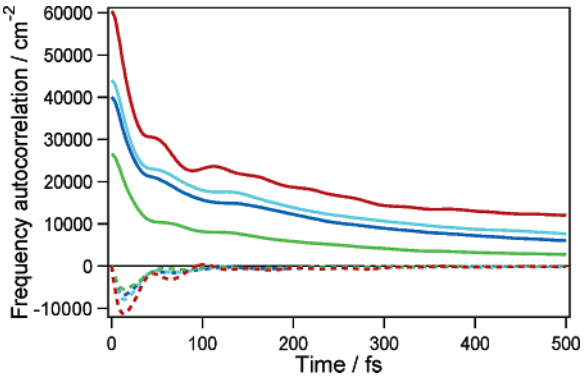

Figure 10. Correlation function of ω_{am} for four different force fields used in the MD simulation and the calculation of the electrostatic potential. The solid lines represent the real part of the correlation function, and the dashed lines represent the imaginary part. Green: SW; blue: TIP4P model; light blue: SPC/E model; red: SWM4 model.

TABLE 9: Parameters for the Frequency Correlation Function Fit to Eq 26

	SPC/E	TIP4P	SW	SWM4
A_1/cm^{-2}	7076	9323	5962	6599
T_1/fs	558	311	402	115027
A_2/cm^{-2}	8754	6218	1653	13112
T_2/fs	90.3	65.1	110.8	251.1
A_3/cm^{-2}	5233	4972	8117	6707
Ω/fs^{-1}	0.205	0.207	0.000	0.107
T_3/fs	8.74	8.53	10.81	16.97
A_4/cm^{-2}	4286	4066	0	6707
Ω'/fs^{-1}	0.073	0.068	0.000	0.036
T_4/fs	24.4	31.0	0.0	47.1

obtained for SWM4 are about half of what is observed for SPC/E and TIP4P.

The simulated infrared absorption line shape of the O−H stretch fundamental for the four force fields is compared with the experiment[13] in Figure 11. The parameters are tabulated in Table 10 along with the experiment and earlier simulations. SW

TABLE 10: Statistics of the Simulated and Experimental Infrared Lineshape of O−H Stretch Fundamental Transition ($g \rightarrow e$)[a]

	TIP4P	SPC/E	SWM4	SW	TIP4P[b]	SPC/E[c]	TIP4P[d]	SPC/E[d]	exp[e]
$\langle\omega\rangle$	3433.7	3446.0	3367.3	3443.6			3445	3418	
$\langle\delta\omega^2\rangle$	22616	23455	33061	14412					
peak position	3419.1	3431.3	3348.1	3430.0	3395				3401
solvent shift	−287.9	−275.7	−358.9	−277.0	−312	−212	−262	−289	−306
Stokes shift	54.8	55.4	78.2	34.6	56				70
fwhm	309.6	315.3	372.6	221.4	160	130	244	293	250
SLE solvent shift	−236.1	−220.0	−289.6	−236.5					
SLE fwhm	310.8	305.1	362.2	221.2					

[a] The first two rows show the ensemble average and the variance of the frequency trajectories. $\langle\delta\omega^2\rangle$ is given in cm^{-2} and the other parameters are in cm^{-1}. [b] Calculation using second class simulation.[69] [c] Calculation using second class simulation.[43] [d] Calculations using an empirical relation between the frequency and electric field.[44] [e] Experimental data for peak position, fwhm are obtained from the data of Fecko et al.,[13] experimental Stokes shift is from ref 14, and experimental gas-phase peak position is from ref 99. The last two lines show the results obtained with the SLE all other numbers are obtained using the cumulant.

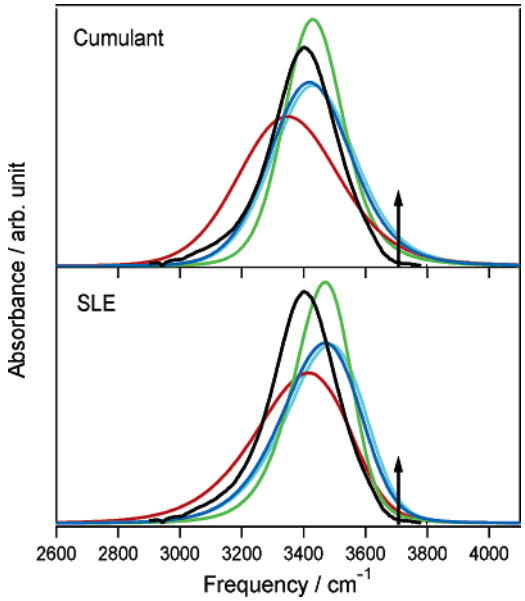

Figure 11. Simulated linear-infrared O−H stretch line shape calculated with the cumulant and the SLE using ω_{am} and ω_{cc}, respectively. The four different force fields are compared with experiment (black).[13] Green: SW model; blue: TIP4P model; light blue: SPC/E model; red: SWM4 model. The black vertical arrow represents the gas-phase frequency.[99]

has the narrowest bandwidth (fwhm: 221 cm^{-1}) and the smallest solvent shift (−277 cm^{-1}) among the four force fields. The infrared band from TIP4P and SPC/E are quite similar in bandwidth (fwhm: 310 and 315 cm^{-1}) and solvent shift (−288 and −276 cm^{-1}). The bandwidth and solvent shift of these three force fields are in good agreement with the experiment (fwhm: 250 cm^{-1}, and solvent shift: 306 cm^{-1}). The SWM4 calculation gives the broadest bandwidth (373 cm^{-1}) and largest solvent shift (−359 cm^{-1}). The calculated Stokes shifts for SPC/E, TIP4P and SW (34 cm^{-1}- 55 cm^{-1}) are smaller than the experiment (70 cm^{-1}),[14] while the Stokes shift for SWM4 (78 cm^{-1}) is slightly larger than the experiment. The TIP4P Stokes shift is very close to the value reported earlier using the same force field.[69]

Compared with the earlier second type of simulations,[43,69] our line shapes are in better agreement with the experiment. The solvent shift does not show a clear improvement. The linewidth and solvent shifts are comparable to those obtained with the third type of simulation using an empirical fit.[44]

V. Identifying the Collective Electrostatic Coordinate

To determine the main variables responsible for the frequency fluctuation and the vibrational line shape of the O−H stretch, the frequency fluctuation should be connected to the electrostatic fluctuation. We define a collective coordinate Q_E for O−H stretch that is linear in the fluctuating part of **C**:

$$Q_E \equiv \Omega_{eq}^{(1)\dagger}\delta\mathbf{C} \tag{27}$$

where $\Omega_{eq}^{(1)}$ was defined in eq 18. By construction the average value of Q_E vanishes $\langle Q_E\rangle = 0$. We then approximate eq 16 as a quadratic polynomial in the collective coordinate Q_E:

$$\omega_{cc} = \omega_{eq} + Q_E - \frac{\kappa}{\omega_{eq}}Q_E^2 \tag{28}$$

Eqs 8 and 16 only differ in the quadratic term. The scatter plot of ω_{am} versus Q_E for TIP4P is displayed in Figure 12. ω_{eq} is 3450.6 cm^{-1} and κ is obtained from a least-squares fit of ω_{am} (eq 16) to the quadratic polynomial of Q_E (eq 28). For TIP4P κ was found to be 1.9116. The resulting polynomial is displayed as a blue curved line in Figure 12. Since the collective coordinate is linear in $\delta\mathbf{C}$, the relationship between the frequency and the electrostatic fluctuation becomes much clearer using that coordinate. The static distribution of Q_E is shown in Figure 14. The distribution of Q_E is very close to a Gaussian. An exact theory for the line shape when ω has a quadratic dependence on a Gaussian variable is given in refs 102 and 103. We have further calculated the linear absorption using the SLE[83−85] following the procedure given in ref 86.

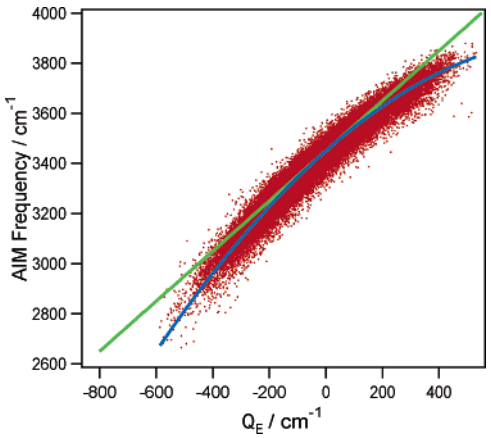

Figure 12. Scattering plot of ω_{am} versus ω_{cc}. The blue curved line is an optimal quadratic polynomial of Q_E (eq 28) ($\omega = 3450.6 + Q_E - 0.000554Q_E^2$). The green line represents the constant plus the linear term in eq 28 with $\kappa = 0$.

The SLE explicitly includes collective coordinants that undergo Markovian dynamics, but are not necessarily Gaussian. It is thus more general than the cumulant expansion. The

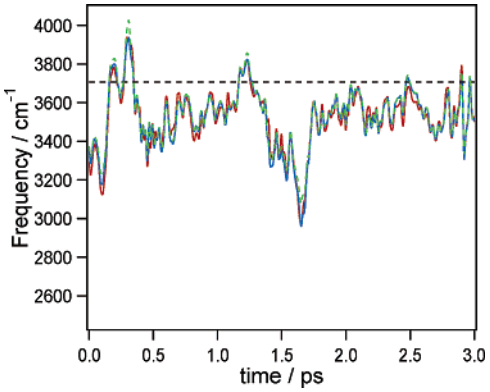

Figure 13. Trajectory of ω_{am} (red), ω_{cc} (blue), and ω_{cc} ($\kappa = 0$) (green dashed) for TIP4P model. The black dashed line is the gas-phase frequency.[99]

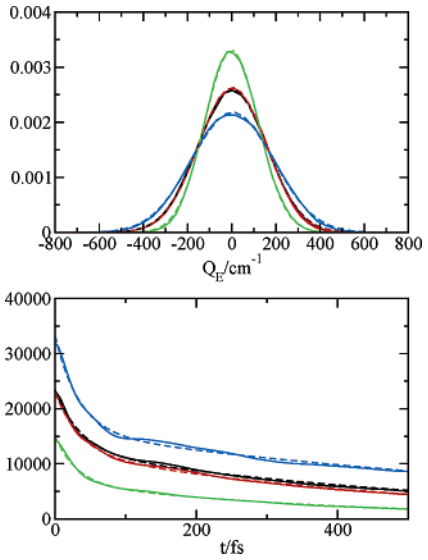

Figure 14. Static distribution (top) and autocorrelation function (bottom) of the collective coordinate Q_E. SPC/E: black, TIP4P: red, SW: green, and SWM4: blue. For the static distribution the Gaussian fits are show with dashed lines. For the correlation functions the biexponential fits are shown with dashed lines.

correlation function of Q_E was modeled by a biexponential decay. The SLE spectrum is shown in Figure 11 and a detailed comparison with the cumulant expansion is given in Supporting Information.

The solvent shift and line width are given in Table 10. If the frequency was linear in the Gaussian collective coordinate Q_E, the cumulant would be exact and the SLE and cumulant simulations will coincide. The small difference in the line shape is due to the finite value of κ. The SLE gives almost the same line width as the cumulant but a smaller solvent shift than both the cumulant and the experiment.

The trajectory of ω_{cc} is shown in Figure 13 together with ω_{am}. The two are virtually identical. The static distribution and correlation function of Q_E for all force fields are displayed in Figure 14. The static distribution is almost Gaussian and the correlations functions are reasonably described by biexponential fits. The infrared line shapes calculated using the trajectory of the ω_{am} and ω_{cc} frequencies are compared in Figure 15. They are almost identical, but the ω_{am} line shape is slightly broader due to the extra fluctuation coming from some of the quadratic terms of eq 16 which are neglected in the ω_{cc} calculation. The infrared line shape obtained by neglecting the quadratic term

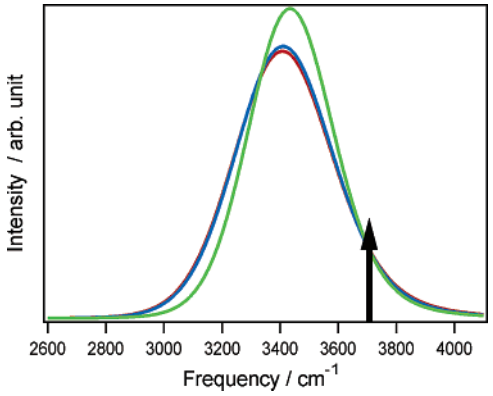

Figure 15. Calculated IR line shape using ω_{am} (red), ω_{cc} (blue), and ω_{cc} ($\kappa = 0$) (green) for the TIP4P model. A black vertical arrow represents the gas-phase frequency.[99]

altogether $\delta\omega_{cc}$ ($\kappa = 0$) is significantly blue shifted and has a narrower bandwidth suggesting the significant contribution of the quadratic term of eq 28.

The solvent frequency shift is

$$\langle \Delta\omega \rangle = \langle \omega \rangle - \omega^{gas} \tag{29}$$

Q_E in the gas phase is

$$Q_E^{gas} = -\Omega_{eq}^{(1)\dagger} \langle \mathbf{C} \rangle \tag{30}$$

Combining eqs 27−30, we get

$$\langle \Delta\omega \rangle \simeq \sum_i \omega_{eq\,i}^{(1)} \langle E_i \rangle - \frac{\kappa}{\omega_{eq}} \sum_{i,j} \omega_{eq\,i}^{(1)} \omega_{eq\,j}^{(1)} (\langle \delta E_i \delta E_j \rangle - \langle E_i \rangle \langle E_j \rangle) \tag{31}$$

The contribution of each electrostatic component to the O−H stretch frequency shift for four force fields is shown in Table 11. The linear terms in eq 31 overestimates the frequency shift by 40−51%, suggesting that the quadratic terms contribute significantly to the shift. In the linear terms, the E_z, E_{xx}, and E_{yy} components are dominant. The significance of E_z and E_{yy} can be attributed to the fact that hydrogen bonding between the oxygen atom of D_2O and hydrogen atom of HOD strongly affects to the O−H stretch frequency. It is interesting that the electric field gradient in the out-of-plane direction (E_{xx}) has a significant contribution (17−26%) to the shift. The hydrogen bonding of D_2O to the oxygen atom of HOD create E_{xx}, and this indicates the importance of hydrogen bonding to the oxygen atom for the O−H stretch vibration.

The time correlation function of the frequency fluctuation are approximated by the correlation function of Q_E,

$$\langle \delta\omega(0)\omega(t) \rangle \simeq \langle Q_E(0) Q_E(t) \rangle \tag{32}$$

Combining with the definition of Q_E (eq 27), we get

$$\begin{aligned} \langle Q_E(0) Q_E(t) \rangle &= \langle \delta\mathbf{C}(0)^{\dagger} \Omega_{eq}^{(1)}\, \Omega_{eq}^{(1)\dagger} \delta\mathbf{C}(t) \rangle \\ &= \sum_{i,j} \omega_{eq\,i}^{(1)} \omega_{eq\,j}^{(1)} \langle \delta E_i(0) \delta E_j(t) \rangle \end{aligned} \tag{33}$$

Using eq 33, the main contribution of each cross- and autocorrelation of the electrostatic components to the O−H stretch frequency fluctuation, $\langle \delta\omega^2 \rangle$ is summarized in Table 12. The most important components are $\langle \delta E_{yy} \delta E_{yy} \rangle$ (28−31%) and $\langle \delta E_{yz} \delta E_{yz} \rangle$ (24−32%). The fluctuation of the electric field

TABLE 11: Contribution of Each Electrostatic Component to the O−H Stretch Fundamental Frequency Shift from the Gas Phase Value

	TIP4P				SPC/E				SWM4				SW			
i	$\omega_i^{(1)\,a}$	$\langle E_i\rangle^b$	$\langle\Delta\omega_i\rangle^c$	(%)^d	$\omega_i^{(1)\,a}$	$\langle E_i\rangle^b$	$\langle\Delta\omega_i\rangle^c$	(%)^d	$\omega_i^{(1)\,a}$	$\langle E_i\rangle^b$	$\langle\Delta\omega_i\rangle^c$	(%)^d	$\omega_i^{(1)\,a}$	$\langle E_i\rangle^b$	$\langle\Delta\omega_i\rangle^c$	(%)^d
x	62	−0.0001	0.0	0.0	67	0.0000	0.0	0.0	75	0.0001	0.0	0.0	65	−0.0001	0.0	0.0
y	9003	0.0000	0.0	0.0	9425	0.0000	0.2	−0.1	10739	−0.0001	−1.4	0.4	9161	0.0002	1.9	−0.7
z	4299	−0.0287	−123.6	45.3	3977	−0.0327	−130.0	49.9	4422	−0.0369	−163.1	48.1	4219	−0.0317	−133.7	50.9
xx	7550	−0.0094	−70.8	26.0	7219	−0.0061	−44.3	17.0	7397	−0.0079	−58.3	17.2	7409	−0.0080	−59.3	22.5
yy	−16671	0.0117	−194.3	71.2	−18845	0.0119	−224.7	86.3	−21405	0.0141	−300.9	88.7	−17297	0.0115	−198.3	75.4
zz	−3397	−0.0023	7.7	−2.8	−2877	−0.0058	16.7	−6.4	−2572	−0.0062	15.9	−4.7	−3591	−0.0035	12.5	−4.7
xy	0	0.0000	0.0	0.0	0	0.0000	0.0	0.0	1	0.0000	0.0	0.0	0	0.0000	0.0	0.0
xz	−1	0.0000	0.0	0.0	1	−0.0001	0.0	0.0	−2	0.0001	0.0	0.0	0	0.0000	0.0	0.0
yz	−17479	0.0000	−0.3	0.1	−17531	0.0001	−1.1	0.4	−19003	0.0001	−2.5	0.7	−17575	0.0000	−0.6	0.2
total			−381.3	139.8			−383.2	147.1			−510.3	150.5			−377.6	143.6

^{a} The units for columns are cm^{-1} au^{-1}. ^{b} The units for columns are au. ^{c} $\langle\Delta\omega_i\rangle \equiv \omega_{\mathrm{eq}\,i}\langle E_i\rangle$ in eq 31. The units for columns are cm^{-1}. ^{d} Columns represent the ratio of the $\langle\Delta\omega_i\rangle$ to the $\langle\delta\omega\rangle$ from the ab initio map in %.

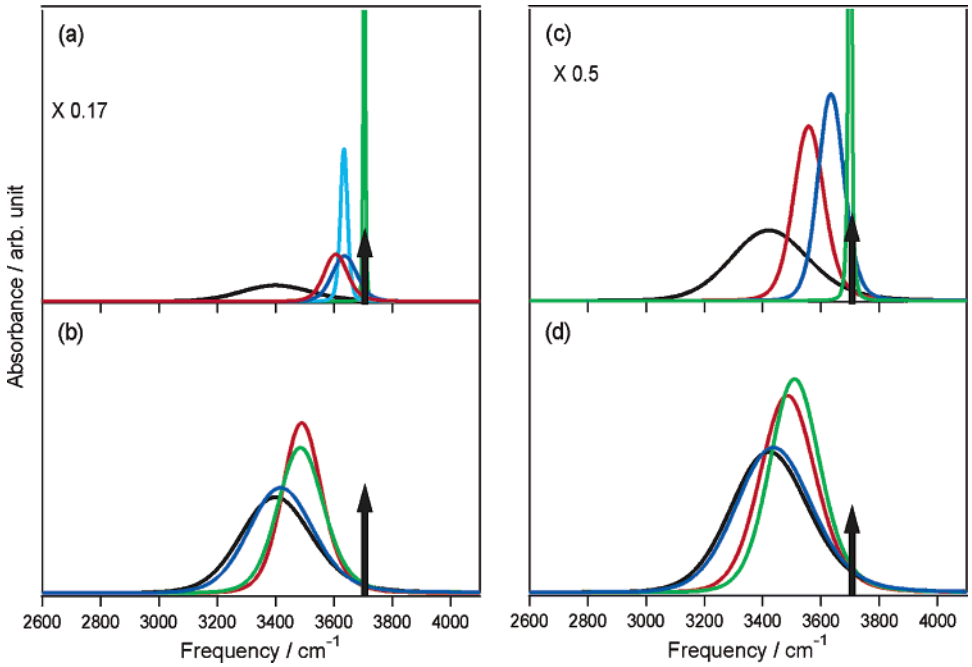

Figure 16. Contributions of various electrostatic components to the simulated infrared line shape using the TIP4P model. Panels (a) and (b) show the contributions of the components represented in the coordinate on the center of the charge (Figure 1a). Panels (c) and (d) show the contributions of the components represented in the coordinate on the hydrogen atom (Figure 1b). Vertical arrow represents the gas-phase frequency,[99] and black lines represent full ω_{am} calculations. In panel (a), red: E_{yy}; green: E_y; blue: E_{xx}; skyblue: E_z. In panel (b), red: E_z and E_{yy}; green: E_z, E_{yy}, and E_y; blue: E_z, E_{yy}, E_y and E_{xx}. In panel (c), green: $E_{z'z'}$; red: $E_{z'z'}$; blue: $E_{x'x'}$. In panel (d) green: $E_{z'z'}$ and $E_{z'z'}$; red: $E_{z'z'}$ and $E_{x'x'}$; blue: $E_{z'}$, $E_{z'z'}$ and $E_{x'x'}$.

parallel to the molecular permanent dipole moment (E_z) which is important for the frequency shift is less important for the frequency fluctuation. The fluctuations related to the electric field gradient in the out-of-plane direction ($\langle\delta E_{xx}\delta E_{xx}\rangle$ and $\langle\delta E_{xx}\delta E_{yy}\rangle$) are also significant (7−13% and 14−22%, respectively).

To analyze the contribution of each electrostatic component to the infrared line shape, the O−H stretch fundamental line shape was calculated by including several combinations of different electrostatic components for TIP4P force field and compared with the line shape with all components (Figure 16 a,b). All line shapes with a single component have a much smaller solvent peak shift and narrower bandwidth than the full calculation (Figure 16a). However, line shapes with E_{yy} and E_{xx} have a significant solvent shift and bandwidth. The infrared band with E_z also has a significant solvent shift but narrower bandwidth. This trend agrees with how these components contribute to the solvent shift $\langle\Delta\omega\rangle$ and the frequency variance $\langle\delta\omega^2\rangle$. The infrared line shape obtained by including both E_z and E_{yy} has a much larger solvent shift and a broader line width than the single component calculation, but is still significantly blue shifted and narrower than the full calculation. Adding E_y contributes less significantly and only to the bandwidth. By adding E_{xx} to these three components, the line shape with E_y, E_z, E_{xx}, and E_{yy} (blue line in Figure 16a) becomes quite close to the full ab initio map calculation. Based on these, the truncated collective coordinate is finally given by

$$Q_E = 175.2\frac{\mathrm{cm}^{-1}}{\frac{\mathrm{V}}{\mathrm{\AA}}}\delta E_y + 83.6\frac{\mathrm{cm}^{-1}}{\frac{\mathrm{V}}{\mathrm{\AA}}}\delta E_z + 77.7\frac{\mathrm{cm}^{-1}}{\frac{\mathrm{V}}{\mathrm{\AA}^2}}\delta E_{xx} - 171.5\frac{\mathrm{cm}^{-1}}{\frac{\mathrm{V}}{\mathrm{\AA}^2}}\delta E_{yy} \quad (34)$$

Scatter plots of the frequencies with these electrostatic components versus the full component calculations for TIP4P force field are shown in Figure 17. The frequencies calculated with the E_y, E_z, and E_{yy} components are systematically higher

TABLE 12: Main Contribution of the Electrostatic Autocorrelation and Crosscorrelation to the O−H Stretch Fundamental Frequency Fluctuation

	TIP4P				SPC/E				SWM4				SW			
i, j	$\omega_i^{(1)}\omega_j^{(1)a}$	$\langle \delta E_i \delta E_j \rangle^b$	$\langle \delta\omega^2 \rangle_{ij}{}^c$	(%)^d	$\omega_i^{(1)}\omega_j^{(1)a}$	$\langle \delta E_i \delta E_j \rangle^b$	$\langle \delta\omega^2 \rangle_{ij}{}^c$	(%)^d	$\omega_i^{(1)}\omega_j^{(1)a}$	$\langle \delta E_i \delta E_j \rangle^b$	$\langle \delta\omega^2 \rangle_{ij}{}^c$	(%)^d	$\omega_i^{(1)}\omega_j^{(1)a}$	$\langle \delta E_i \delta E_j \rangle^b$	$\langle \delta\omega^2 \rangle_{ij}{}^c$	(%)^d
y, y	81.05	43.06	3489	15.4	88.83	43.70	3881	16.5	115.33	68.65	7917	23.8	83.92	41.33	3468	23.9
y, yy	−150.08	−0.07	20	0.1	−177.61	−0.13	47	0.2	−229.87	−0.14	64	0.2	−158.45	−0.04	13	0.1
y, yz	−157.35	15.08	−4745	−20.9	−165.22	14.56	−4811	−20.4	−204.07	21.28	−8685	−26.1	−161.01	9.65	−3109	−21.4
z, z	18.48	50.61	935	4.1	15.82	48.83	772	3.3	19.56	87.57	1713	5.2	17.80	54.51	970	6.7
z, yy	−71.67	−9.93	1423	6.3	−74.95	−11.89	1782	7.6	−94.66	−20.89	3955	11.9	−72.98	−8.54	1246	8.6
z, zz	−14.60	16.35	−478	−2.1	−11.44	12.76	−292	−1.2	−11.37	28.24	−642	−1.9	−15.15	11.42	−346	−2.4
xx, xx	57.00	53.53	3051	13.4	52.12	39.38	2053	8.7	54.71	43.60	2385	7.2	54.90	24.17	1327	9.1
xx, yy	−125.86	−19.77	4978	21.9	−136.05	−15.82	4304	18.3	−158.33	−16.03	5078	15.3	−128.15	−8.14	2087	14.4
yy, yy	277.92	19.77	5494	24.2	355.13	19.73	7006	29.7	458.16	23.00	10539	31.7	299.17	13.13	3928	27.1
yy, yz	291.38	0.04	24	0.1	330.37	0.10	65	0.3	406.75	−0.73	−595	−1.8	304.00	0.09	55	0.4
zz, zz	11.54	33.74	389	1.7	8.28	27.48	227	1.0	6.61	34.53	228	0.7	12.90	21.01	271	1.9
yz, yz	305.50	20.50	6264	27.6	307.33	23.64	7264	30.8	361.10	28.05	10128	30.5	308.90	13.66	4218	29.1
total			20845	91.7			22298	94.6			32086	96.6			14128	97.3

[a] The units for columns are 10^{-6} cm^{-2} au^{-2} (*a*), 10^6 au^2 (*b*), and cm^{-2} (*c*). In columns *c* $\langle \delta\omega^2 \rangle_{ij} \equiv \omega_{eq}^{(1)}\omega_{eq}^{(1)}\langle \delta E_i \delta E_j \rangle$ in eq 33. Columns *d* represent the ratio of the $\langle \delta\omega^2 \rangle_{ij}$ to the $\langle \delta\omega^2 \rangle$ from the ab initio map in %.

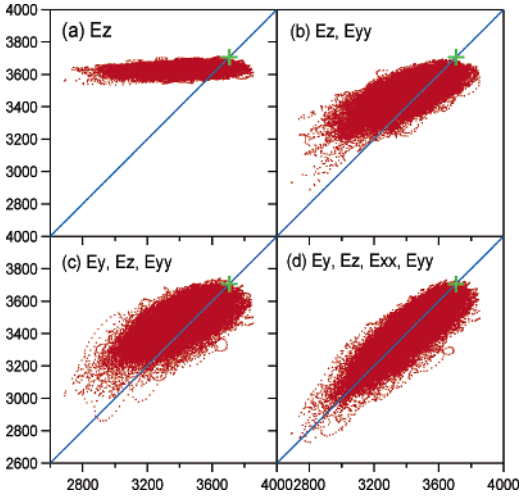

Figure 17. Scatter plots of the frequencies calculated with various electrostatic components versus the full ω_{am}. Electrostatic components are represented with the coordinate at the center of charge. Green markers represent the gas-phase frequency,[99] and blue lines are $\omega = \omega_{am}$ lines. (a): E_z component; (b): E_z and E_{yy} components; (c): E_y, E_z, and E_{yy} components; (d): E_y, E_z, E_{yy}, and E_{xx} components. All axes are in cm^{-1}.

than the all component calculation (Figure 17c), whereas when E_{xx} is included, we obtain an excellent correlation (Figure 17d).

VI. The Collective Coordinate in a Bond Oriented Frame

Earlier works found a correlation between the O−H stretch frequency and the electric field on the H atom in the O−H bond direction, and the frequency fluctuations were calculated using an empirical relation.[7,44] This correlation is reasonable because the hydrogen atom moves primarily along the O−H stretch. We have therefore examined the actual contribution of the electric field on the hydrogen atom in that direction to the frequency fluctuation. We calculated the O−H stretch frequency with any components of the electrostatic potential expanded at an arbitrary position by a transformation of the ab initio electrostatic map expressed in eq 12 (Appendix C). We used a coordinate system fixed on the hydrogen atom with the z'-axis parallel to the O−H bond and x' perpendicular to the molecular plane (Figure 1b). The ab initio map and the electrostatic components are transformed using eq C7 with three parameters defined in Figure 1c (TIP4P, SW, SWM4: $\Delta y = -0.7567$ Å, $\Delta z = -0.4687$ Å, $\theta = 52.26$; SPC/E: $\Delta y = -0.8167$ Å, $\Delta z = -0.4617$ Å, $\theta = 54.75$ deg). Since the $x'-y'$ plane in the new coordinate system is the same as the $x-y$ plane in the original coordinate, $E_{x'x'}$ is identical to E_{xx} (eq C2 in Appendix C).

The contribution of each auto- and crosscorrelation of electrostatic components to the frequency variance $\langle \delta\omega^2 \rangle$ is tabulated in Table 13. The autocorrelation function of the electric field component parallel to the O−H bond ($E_{z'}$) has the largest contribution (41−52%), and the crosscorrelation of $E_{z'}$ and the two diagonal gradient components ($E_{x'x'} = E_{xx}$ and $E_{z'z'}$) have significant contributions (16−24% and 13−16%). The truncated collective coordinate in this system is

$$Q_E = 189.7\frac{\text{cm}^{-1}}{\frac{\text{V}}{\text{Å}}}\delta E_{z'} + 77.7\frac{\text{cm}^{-1}}{\frac{\text{V}}{\text{Å}^2}}\delta E_{x'x'} - 39.5\frac{\text{cm}^{-1}}{\frac{\text{V}}{\text{Å}^2}}\delta E_{z'z'} \quad (35)$$

To analyze these three ($E_{z'}$, $E_{z'z'}$, and $E_{x'x'}$) electrostatic contributions to the line shape, the O−H stretch fundamental

TABLE 13: Main Contribution of the Electrostatic Autocorrelation and Crosscorrelation to the O−H Stretch Fundamental Frequency Fluctuation

	TIP4P				SPC/E			SWM4			SW		
i,j	$\omega_i^{(1)}\omega_j^{(1)a}$	$\langle\delta E_i\delta E_j\rangle^b$	$\langle\delta\omega^2\rangle_{ij}$,^{c}	(%)^d	$\omega_i^{(1)}\omega_j^{(1)a}$	$\langle\delta E_i\delta E_j\rangle^b$	$\langle\delta\omega^2\rangle_{ij}$	(%)^d	$\omega_i^{(1)}\omega_j^{(1)a}$	$\langle\delta E_i\delta E_j\rangle^b$	$\langle\delta\omega^2\rangle_{ij}$	(%)^d	$\omega_i^{(1)}\omega_j^{(1)a}$	$\langle\delta E_i\delta E_j\rangle^b$	$\langle\delta\omega^2\rangle_{ij}$	(%)^d
y,y'	4.45	65.55	292	1.3	4.80	76.01	365	1.5	9.46	88.81	840	2.5	5.16	63.38	327	2.3
$y,x'x'$	15.93	−1.24	−39	−0.2	15.82	−1.99	−63	−0.3	22.75	1.08	49	0.1	16.82	−1.86	−63	−0.4
$y,y'z'$	−6.81	−15.11	206	0.9	−7.79	−19.76	308	1.3	−19.56	−15.75	616	1.9	−7.59	−12.35	187	1.3
z,z'	95.08	97.79	9297	40.9	99.84	112.03	11186	47.5	125.42	131.28	16466	49.5	96.57	77.78	7511	51.7
$z,x'x'$	73.62	37.38	5503	24.2	72.14	31.56	4554	19.3	82.84	27.92	4625	13.9	72.81	16.23	2363	16.3
$z,z'z'$	−37.46	−40.97	3070	13.5	−41.61	−45.23	3764	16.0	−53.84	−44.58	4800	14.4	−41.52	−24.08	2000	13.8
$z,y'z'$	−31.48	−4.42	278	1.2	−35.51	−4.67	331	1.4	−71.22	−12.75	1817	5.5	−32.83	−5.61	368	2.5
$x'x',x'x'$	57.00	53.53	3051	13.4	52.12	39.38	2053	8.7	54.71	43.60	2385	7.2	54.90	24.17	1327	9.1
$x'x',y'y'$	3.47	−28.25	−196	−0.9	3.30	−20.89	−138	−0.6	0.81	−23.81	−38	−0.1	1.33	−13.01	−35	−0.2
$x'x',z'z'$	−29.01	−25.27	1466	6.5	−30.06	−18.49	1112	4.7	−35.56	−19.79	1408	4.2	−31.31	−11.15	698	4.8
$x'x',y'z'$	−24.38	6.83	−333	−1.5	−25.66	3.69	−189	−0.8	−47.04	5.44	−511	−1.5	−24.75	3.83	−190	−1.3
$z'z',z'z'$	14.76	31.91	471	2.1	17.34	31.22	541	2.3	23.11	36.10	834	2.5	17.85	18.64	333	2.3
$y'z',y'z'$	10.43	13.87	145	0.6	12.63	14.83	187	0.8	40.44	18.73	757	2.3	11.16	11.17	125	0.9
total			23210	102.1			24011	101.9			34048	102.5			14952	103.0

^{a} The units for columns are 10^{-6} cm^{-2} au^{-2}. ^{b} The units for columns are 10^6 au^2. ^{c} $\langle\delta\omega^2\rangle_{ij} \equiv \omega_{eq\,i}^{(1)}\omega_{eq\,j}^{(1)}\langle\delta E_i\delta E_j\rangle$ in eq 33. The units for columns are cm^{-2}. ^{d} Columns represent the ratio of the $\langle\delta\omega^2\rangle_{ij}$ to the $\langle\delta\omega^2\rangle$ from the ab initio map in %.

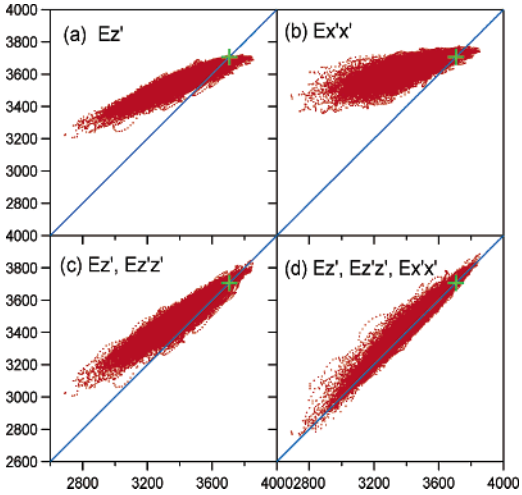

Figure 18. Scatter plots of the frequencies calculated with various electrostatic components versus the full ω_{am}. Electrostatic components are represented with the coordinate at the H atom. Green markers represent the gas-phase frequency,[99] and blue lines are $\omega = \omega_{am}$ lines. (a): $E_{z'}$ component; (b): $E_{x'x'}$ component; (c): $E_{z'}$, $E_{z'z'}$ components; (d): $E_{z'}$, $E_{z'z'}$, $E_{x'x'}$ components. All axes are in cm^{-1}.

infrared line shape was calculated for TIP4P including these electrostatic components (Figure 16c,d). The infrared line shape obtained using $E_{z'}$ (the green solid line in Figure 16c) gives a much smaller frequency shift and narrower bandwidth. Including the gradient ($E_{z'z'}$) improves the result significantly (red solid line in Figure 16d), but the resulting solvent peak shift and the bandwidth are still smaller than the full calculation. Adding $E_{x'x'}$ to these two components gives a comparison with the full calculation (blue solid line in Figure 16d). The line shape cannot be reproduced by only the electric field parallel to the O−H bond. All three electrostatic components (the electric field parallel to the O−H bond, its gradient in the same direction, and the diagonal out-of-plane electric field gradient) make a significant contribution to the infrared line shape. The simulated line shape using all three components is in a good agreement with the full ab initio map. This is supported by the scatter plot of the frequencies with these three electrostatic components versus the full component calculations for TIP4P force field shown in Figure 18. The frequencies calculated with only the E_z (Figure 18a) component are systematically higher than the full (Figure 18c), indicating the significant contribution of $E_{z'z'}$ and $E_{x'x'}$ to the O−H stretch frequency.

VII. Discussion

We have constructed an ab initio electrostatic map for the infrared spectra of HOD in D_2O, in which the fundamental O−H stretch vibrational frequency, the overtone, and the transition dipole moments are parametrized with the electric field and its gradients at the HOD center of charge. The map was created by numerical derivatives of the force calculations in the presence of an electric field or an electric field gradient. This required a modification of the Gaussian 03 code to carry out the force calculations in the presence of electric field gradients and higher order derivatives (up to third order). We expanded the vibrational potential energy surface to sixth order in the three normal coordinates (O−H stretch, O−D stretch, and H−O−D bending).

The simulation strategy based on the ab initio electrostatic map has several advantages. First, once these vibrational quantities are parametrized with the electrostatic potential, the map can be used to calculate the transition frequencies and transition dipole moments from a MD trajectory at a low

computational cost, avoiding repeated ab initio calculations. Second, since the model is purely electrostatic, the parameters of the specific solute are transferable and can be used for any solvent and force field.

The electric field and its gradients were calculated from the molecular dynamics simulation using 4 different force fields (TIP4P, SPC/E, SWM4, SW). The autocorrelation of the electric field parallel to the molecular dipole moment (E_z) decays monotonically with a platau at 80 fs, the autocorrelation of the other two directions (E_x and E_y) show damped oscillatory behavior. This suggests that E_z is dominated by the reaction field induced by the global response of the solute molecules, the other directions correspond to the ocillation of the HOD molecule in the D_2O solvent cage. The oscillation frequency and the damping in the x and y direction vary for the four different models, suggesting different dynamics of the HOD molecule in the solvent cage.

The calculations of the O−H stretch infrared line shape from the nonpolarizable force field (TIP4P and SPC/E) give the similar peak shifts and bandwidths. The two polarizable force fields (SWM4 and SW) give the two extreme results. The infrared bandwidth of SW is the narrowest (fwhm: 221 cm^{-1}), TIP4P and SPC/E bandwidths are similar (310 and 315 cm^{-1}) and broader than the SW one. The experimental bandwidth (250 cm^{-1}) is between the two nonpolarizable force fields (TIP4P and SPC/E) and the SW force field. SWM4 gives the broadest bandwidth (373 cm^{-1}). SW gives the smallest Stokes shift (34.6 cm^{-1}), and SWM4 gives the largest value (78.2 cm^{-1}). Overall, three of the force fields (TIP4P, SPC/E, and SW) give the O−H stretch infrared line shape in good agreement with the experiment, demonstrating that the vibrational band for the hydrogen bonding system can be adequately described by an electrostatic model. This implies that covalent interactions in hydrogen bonding, collisions, exchange, and charge transfer are less important for the line shapes.

The significant difference in the simulated bandwidths and Stokes shifts using the four force fields (221−373 cm^{-1} and 34.6−78.2 cm^{-1}) shows the sensitivity of the vibrational response to the force field and suggests the necessity to develop the optimal force field designed for both inter- and intramolecular dynamics. Especially the opposite contribution of the polarization to the solvent peak shift and the bandwidth in the two polarizable force fields (broader and red shifted in SWM4, and narrower and blue shifted in SW) show the significance of the polarization to the O−H stretch. Infrared line shapes can thus be used to refine the polarizable force field parameters.

We identified a collective coordinate Q_E as a linear combination of the electrostatic components by linearizing the map at the average of electrostatic components. The frequency correlation function and the infrared line shape are well reproduced by that coordinate alone. By decomposing this collective coordinate into a two Markovian collective coordinates the linear absorption was computed using the SLE. Since the collective coordinate has a Gaussian distribution and the quadratic contribution κ is small, the SLE is similar to the cumulant. Using that coordinate, the frequency shift and frequency fluctuation were decomposed into the contribution of each electrostatic component for four force fields. The electric field parallel to the molecular dipole moment (E_z) and the electric field gradient parallel to the vector connecting hydrogen and deuterium (E_{yy}) contribute most to the frequency shift (46−51 and 71−89%). The diagonal gradient of the out-of-plane electric field E_{xx} is also significant (17−26%). $\langle \delta\omega^2 \rangle$ is attributed mostly to the cross- and autocorrelation of E_y, E_{yy}, and E_{xx}. The contribution of $\langle E_z^2 \rangle$ is relatively small (3−7%), This is connected to the fact that the electric field parallel to the molecular dipole moment is created by the global dielectric response of the D_2O solvents and thus has the largest average absolute value (0.028−0.037) but a smaller amplitude of fluctuation. The calculated infrared line shapes including all these four components E_z, E_y, E_{yy}, and E_{xx} are in good agreement with the full component calculation. Fewer components are not sufficient.

We identified the main electrostatic components responsible for the infrared line shape in the coordinate system on the hydrogen atom with z' -axis parallel to the O−H bond and x' perpendicular to the molecular plane (Figure 1b). By analyzing the contribution of each component to the static frequency variance $\langle \delta\omega^2 \rangle$, three components (electric field in O−H bond direction: E'_z, the diagonal gradient of the electric field in O−H bond direction: $E_{z'z'}$, and the diagonal gradient of the out-of-plane electric field: $E_{x'x'} = E_{xx}$) were found to be important. The infrared line shapes obtained using these three components are in good agreement with the full calculation. The infrared line shape obtained using only the electric field in O−H bond direction (E'_z) has a much smaller peak shift with respect to the gas phase and a much narrower bandwidth compared to the full components calculation suggesting that the E'_z can explain only a part of the O−H stretch frequency fluctuation and line shape. Analysis of the electrostatic contributions to the O−H stretch fundamental infrared line shape in both coordinate systems shows the significance of E_{xx} (= $E_{x'x'}$) to the O−H stretch vibration which was neglected in earlier works.[7,44] E_{xx} corresponds to the hydrogen bonding of oxygen of HOD to the deuterium of D_2O solvent. The partial charge of deuterium of D_2O creates the diagonal negative gradient of the out-of-plane electric field, and simulated ensemble average values of $\langle E_{xx} \rangle$ ($-0.0061 \sim -0.0091$) coincide with this physical picture. The simulated infrared line shapes with and without E_{xx} in addition to the other three (E_z, E_y, E_{yy}) and two components ($E_{z'}$, $E_{z'z'}$) in the two coordinate systems directly show the significance of E_{xx} contribution to the line shape.

The present approach provides a physical picture of the OH stretch in terms of the response of a chromophore to an external electric field, and reproduces its line shape and peak shift. The parametrized fundamental transition frequency (ω_{ge}), the overtone (ω_{gf}) anharmonicity as well as transition dipoles can be used in the modeling of nonlinear spectra.

Acknowledgment. The support of the National Institutes of Health Grant No. (RO1 GM59230-04) and the National Science Foundation Grant No. (CHE-0132571) is gratefully acknowledged. We wish to thank Dr. Mike Frisch and Dr. So Hirata for most useful discussions regarding the modification of the Gaussian 03 code, and Prof. Andrei Tokmakoff for providing his experimental data.

Appendix A: Potential Energy Gradient Calculation in the Presence of a Nonuniform Electric Field

The potential energy gradient (force) calculation is implemented in the current version (B.04, B.05, and C.01) of the Gaussian 03 program only with a uniform electric field. We implemented the potential energy gradient (force) calculation in the presence of up to fourth derivatives of the electrostatic potential for the future purpose. The electrostatic potential induced by the solvent is expanded around the center of charge to quartic order:

$$U(\mathbf{X}) = U_0 - \sum_{\alpha=1}^{3} E_\alpha X_\alpha - \sum_{\alpha,\beta=1}^{3} E_{\alpha\beta} X_\alpha X_\beta - \sum_{\alpha,\beta,\gamma=1}^{3} E_{\alpha\beta\gamma} X_\alpha X_\beta X_\gamma - \sum_{\alpha,\beta,g,\delta=1}^{3} E_{\alpha\beta\gamma\delta} X_\alpha X_\beta X_\gamma X_\delta \quad \text{(A1)}$$

where X_α, X_β, X_γ, X_δ represent Cartesian components x, y, or z, and $E_{\alpha_1\cdots\alpha_n}$ is

$$E_{\alpha_1\cdots\alpha_n} \equiv -\frac{1}{n!}\left(\frac{\partial U}{\partial X_{\alpha_1}\cdots\partial X_{\alpha_n}}\right) \quad \text{(A2)}$$

The electrostatic solvent solute potential is

$$H_{es} = \sum_{a=1}^{N_{nuclei}} Z_a U_{es}(\mathbf{R}_a) - \sum_{i=1}^{N_{electrons}} eU_{es}(\mathbf{r}_i) \quad \text{(A3)}$$

where e is the electron charge and Z_a is the nuclear charge. $\mathbf{R}_a$ is the nuclear coordinates and $\mathbf{r}_i$ are the electronic coordinates. Combining aqs A1 and A3, we get

$$H_{es} = H_{nuc} + H_{el} \quad \text{(A4)}$$

where

$$H_{nuc} = -\sum_{a=1}^{N_{nuclei}} Z_a\Big(\sum_{\alpha=1}^{3} E_\alpha R_{a\alpha} + \sum_{\alpha,\beta=1}^{3} E_{\alpha\beta} R_{a\alpha} R_{a\beta} + \sum_{\alpha,\beta,\gamma=1}^{3} E_{\alpha\beta\gamma} R_{a\alpha} R_{a\beta} R_{a\gamma} + \sum_{\alpha,\beta,\gamma,\delta=1}^{3} E_{\alpha\beta\gamma\delta} R_{a\alpha} R_{a\beta} R_{a\gamma} R_{a\delta}\Big) \quad \text{(A5)}$$

$$H_{el} = e\sum_{i=1}^{N_{electrons}}\Big(\sum_{\alpha=1}^{3} E_\alpha r_{i\alpha} + \sum_{\alpha,\beta=1}^{3} E_{\alpha\beta} r_{i\alpha} r_{i\beta} + \sum_{\alpha,\beta,\gamma=1}^{3} E_{\alpha\beta\gamma} r_{i\alpha} r_{i\beta} r_{i\gamma} + \sum_{\alpha,\beta,\gamma,\delta=1}^{3} E_{\alpha\beta\gamma\delta} r_{i\alpha} r_{i\beta} r_{i\gamma} r_{i\delta}\Big) \quad \text{(A6)}$$

The nuclear part H_{nuc} is a polynomial in the nuclear coordinates and its derivatives with respect to the nuclear position is given by

$$\frac{\partial H_{nuc}}{\partial R_{a\beta}} = Z_a \sum_{m=1}^{4} E_{\alpha_1\cdots\alpha_m} \sum_{i=1}^{m} \prod_{j\neq i} R_{a\alpha_j} \delta_{\beta\alpha_i} \quad \text{(A7)}$$

where $\delta_{\beta\alpha_i}$ is a kronecker δ function. The expectation value of the electron part H_{el} is obtained by

$$\langle H_{el}\rangle = \langle\psi|H_{el}|\psi\rangle \quad \text{(A8)}$$

where ψ is the many-electron wave function. Combining eqs A6 and A8 and using single-electron atomic orbitals, the electron part becomes:

$$\langle H_{el}\rangle = e\sum_{n=1}^{4}\sum_{\alpha_1=1}^{3}\cdots\sum_{\alpha_n}^{3} E_{\alpha_1\cdots\alpha_n} \sum_{b,c,\nu,\nu'} P_{b\nu,c\nu'} \langle\phi_{b\nu}|\prod_{i=1}^{n} r_{\alpha_i}|\phi_{c\nu'}\rangle \quad \text{(A9)}$$

where $\phi_{b\nu}$ and $\phi_{c\nu'}$ are νth and ν'th one-electron Gaussian atomic orbitals on nuclei b and c. $P_{b\nu,c\nu'}$ is the single electron density matrix. The derivative of the electron part with respect to the coordinate of nucleus a,$R_{a\beta}$ ($\beta = x$, y, or z) is

$$\frac{\partial\langle H_{el}\rangle}{\partial R_{a\beta}} = \left.\frac{\partial\langle H_{el}\rangle}{\partial R_{a\beta}}\right|_{P_{b\nu,c\nu'}=\text{const.}} + \sum_{b,c,\nu,\nu'} \frac{\partial\langle H_{el}\rangle}{\partial P_{b\nu,c\nu'}} \frac{\partial P_{b\nu,c\nu'}}{\partial R_{a\beta}} \quad \text{(A10)}$$

Here the second term is already implemented in the Gaussian 03 program using the energy-weighted density matrix.[104−106] The first term becomes

$$\left.\frac{\partial\langle H_{el}\rangle}{\partial R_{a\beta}}\right|_{P_{\nu\nu,c\nu'}=\text{const}} = e\sum_{n=1}^{4}\sum_{\alpha_1=1}^{3}\cdots\sum_{\alpha_n}^{3} E_{\alpha_1\cdots\alpha_n} \sum_{b,c,\nu,\nu'} P_{b\nu,c\nu'} \times \left(\left\langle\frac{\partial\phi_{b\nu}}{\partial R_{b\beta}}\right|\prod_{i=1}^{n} r_{\alpha_i}\left|\phi_{c\nu'}\right\rangle\delta_{ba} + \left\langle\phi_{b\nu}\right|\prod_{i=1}^{n} r_{\alpha_i}\left|\frac{\partial\phi_{c\nu'}}{\partial R_{c\beta}}\right\rangle\delta_{ca}\right) \quad \text{(A11)}$$

Using a following identical equation:

$$\prod_{i=1}^{n} r_{\alpha_i} = \prod_{i=1}^{n}(r_{\alpha_i} - R_{b\alpha_i}) + \sum_{i=1}^{n} R_{b\alpha_i}\prod_{j\neq i}(r_{\alpha_j} - R_{b\alpha_j}) \quad \text{(A12)}$$

and considering the invariance with respect to the simultaneous translation of both $\phi_{b\nu}$ and $\phi_{c\nu'}$:

$$\left\langle\frac{\partial\phi_{b\nu}}{\partial R_{b\alpha}}\right|\phi_{c\nu'}\right\rangle + \left\langle\phi_{b\nu}\left|\frac{\partial\phi_{c\nu'}}{\partial R_{c\alpha}}\right\rangle\right. = 0 \quad \text{(A13)}$$

we get,

$$\left\langle\frac{\partial\phi_{b\nu}}{\partial R_{b\beta}}\right|\prod_{i=1}^{n} r_{\alpha_i}\left|\phi_{c\nu'}\right\rangle = -\left\langle\phi_{b\nu}\left|\prod_{i=1}^{n} r_{\alpha_i}\right|\frac{\partial\phi_{c\nu'}}{\partial R_{c\beta}}\right\rangle + \sum_{i=1}^{n}\delta_{\beta\alpha_i}\langle\phi_{b\nu}|\prod_{j\neq i}(r_{\alpha_j} - R_{b\alpha_j})|\phi_{c\nu'}\rangle \quad \text{(A14)}$$

Combining eqs A11 and A14, the final expression for the partial derivative of the electron part with the nuclear coordinate $R_{a\beta}$ becomes:

$$\left.\frac{\partial\langle H_{el}\rangle}{\partial R_{a\beta}}\right|_{P_{b\nu,c\nu'}=\text{const}} = e\sum_{n=1}^{4}\sum_{\alpha_1=1}^{3}\cdots\sum_{\alpha_n=1}^{3} E_{\alpha_1\cdots\alpha_n} \sum_{b,c,\nu,\nu'} P_{b\nu,c\nu'} \times \left(-\left\langle\phi_{b\nu}\left|\Pi_{i=1}^{n} r_{\alpha_i}\right|\frac{\partial\phi_{c\nu'}}{\partial R_{c\beta}}\right\rangle\delta_{ba} + \sum_{i=1}^{n} S_{\nu\nu',i}\delta_{\beta\alpha_i}\delta_{ba} + \left\langle\phi_{b\nu}\left|\Pi_{i=1}^{n} r_{\alpha_i}\right|\frac{\partial\phi_{c\nu'}}{\partial R_{c\beta}}\right\rangle\delta_{ca}\right) \quad \text{(A15)}$$

where $S_{\nu\nu',i}$ is an overlap integral defined as

$$S_{\nu\nu',i} \equiv \langle\phi_{b\nu}\Pi_{j\neq i}(r_{\alpha_j} - R_{b\alpha_j})|\phi_{c\nu'}\rangle \quad \text{(A16)}$$

Only the uniform electric field part ($n = 1$) in eqs A7 and A15 are implemented in the original Gaussian 03 program, and we implemented the summation over $n = 2-4$ in these equations. The bra orbital in eq A16, $\langle\phi_{b\nu}\Pi_{j\neq i}(r_{\alpha_j} - R_{b\alpha_j})|$ is also a Gaussian orbital with a higher angular momentum and the overlap S is therefore calculated using a Gaussian routine with the recurrence formulas.[107,108] The ket derivative of the multipole integral $\langle\phi_{b\nu}|r_{\alpha_1}\cdots r_{\alpha_n}|(\partial\phi_{c\nu'}/\partial R_{c\beta})\rangle$ for s, p, d, and f type atomic orbitals is also obtained by subroutines in the Gaussian 03 program.[107,108]

The calculated analytic forces in the presence of several nonuniform electric fields were compared with the numerical forces, and the analytic and numerical forces agree very well.

Appendix B: Numerical Derivative Calculation of the Potential Energy Gradients

The potential energy gradients with respect to the normal coordinates $\mathbf{Q} \equiv (Q_1, Q_2, Q_3)$ at distorted geometries $(\mathbf{Q}_0 + \delta\mathbf{Q}_p)$ around the optimized structure $(\mathbf{Q}_0)$ are expressed:

$$f_{l_1}^{(1)}(\mathbf{Q}_0 + \delta\mathbf{Q}_p) = f_{l1}^{(1)}(\mathbf{Q}_0) + \sum_{n=2}^{6}\sum_{l_2=1}^{3}\cdots\sum_{l_n=1}^{3} f_{l_1 l_2 \cdots l_n}^{(n)} \Pi_{i=2}^{n} \delta Q_{pl_i} \tag{B1}$$

where l_i is the index for the three normal coordinates. $f_{l_1}^{(1)}(\mathbf{Q}_0 + \delta\mathbf{Q}_p)$ is calculated from the analytical energy gradients with respect to the Cartesian coordinate of nuclear positions which is obtained with the ab initio calculation using our modified Gaussian 03 program. Combining with the potential energy gradients at $\mathbf{Q}_0 - \delta\mathbf{Q}_p$, we get:

$$g_{pl_1}^{(1)} = \sum_{n=2,4,6}\sum_{l_2=1}^{3}\sum_{l_4=1}^{3}\sum_{l_6=1}^{3} f_{l_1 l_2 \cdots l_n}^{(n)} \Pi_{i=2}^{n} \delta Q_{pl_i} \tag{B2}$$

$$h_{pl_1}^{(1)} = f_{l_1}^{(1)}(\mathbf{Q}_0) + \sum_{n=3,5}\sum_{l_3=1}^{3}\sum_{l_5=1}^{3} f_{l_1 l_2 \cdots l_n}^{(n)} \Pi_{i=2}^{n} \delta Q_{pl_i} \tag{B3}$$

where

$$g_{pl_1}^{(1)} \equiv (f_{l_1}^{(1)}(\mathbf{Q}_0 + \delta\mathbf{Q}_p) - f_{l_1}^{(1)}(\mathbf{Q}_0 - \delta\mathbf{Q}_p))/2 \tag{B4}$$

$$h_{pl_1}^{(1)} \equiv (f_{l_1}^{(1)}(\mathbf{Q}_0 + \delta\mathbf{Q}_p) + f_{l_1}^{(1)}(\mathbf{Q}_0 - \delta\mathbf{Q}_p))/2 \tag{B5}$$

The expansion coefficients $f_{l_1 \cdots l_n}^{(n)}$ are calculated by solving a linear equation (eqs B2 and B3) of $f_{l_1 \cdots l_n}^{(n)}$ with known parameters $g_{pl_i}^{(1)}$, $h_{pl_i}^{(1)}$, and δQ_{pl_i} for different geometries $\mathbf{Q}_0 + \delta\mathbf{Q}_1$, ..., $\mathbf{Q}_0 + \delta\mathbf{Q}_{n_p}$. A total of 57 different geometries are used to calculate anharmonic force constants up to sixth order.

Appendix C: Coordinate Transformation of the Electrostatic Components

We define a new coordinate system which has the origin located at $(0, \Delta y, \Delta z)$ and is rotated with θ in the $y-z$ plane from the original coordinate system (see Figure 1c). The electrostatic components in the new frame $\mathbf{C}'$ is expressed as a linear transformation of the components in the original frame $\mathbf{C}$:

$$\mathbf{C}' = \mathbf{R}_\mathbf{C}\mathbf{C} \tag{C1}$$

where $\mathbf{R}_\mathbf{C}$ is a 9×9 linear transformation matrix defined as:

$$\mathbf{R}_\mathbf{C} = \begin{pmatrix}
1 & 0 & 0 & 0 & 0 & 0 & \Delta y & \Delta z & 0 \\
0 & \cos\theta & -\sin\theta & 0 & \Delta y \cos\theta & -\Delta z \sin\theta & 0 & 0 & -\Delta y \sin\theta + \Delta z \cos\theta \\
0 & \sin\theta & \cos\theta & 0 & \Delta y \sin\theta & \Delta z \cos\theta & 0 & 0 & \Delta y \cos\theta + \Delta z \sin\theta \\
0 & 0 & 0 & 1 & 0 & 0 & 0 & 0 & 0 \\
0 & 0 & 0 & 0 & \cos^2\theta & \sin^2\theta & 0 & 0 & -2\sin\theta\cos\theta \\
0 & 0 & 0 & 0 & \sin^2\theta & \cos^2\theta & 0 & 0 & 2\sin\theta\cos\theta \\
0 & 0 & 0 & 0 & 0 & 0 & \cos\theta & -\sin\theta & 0 \\
0 & 0 & 0 & 0 & 0 & 0 & \sin\theta & \cos\theta & 0 \\
0 & 0 & 0 & 0 & \cos\theta\sin\theta & -\cos\theta\sin\theta & 0 & 0 & \cos^2\theta - \sin^2\theta
\end{pmatrix} \tag{C2}$$

With the transformation, eq 12 becomes:

$$\omega = \omega^{\mathrm{gas}} + \Omega'^{(1)\dagger}\mathbf{C}' + \frac{1}{2}\mathbf{C}'^{\dagger}\Omega'^{(2)}\mathbf{C}' \tag{C3}$$

where

$$\Omega'^{(1)} = \Omega^{(1)}\mathbf{R}_\mathbf{C}^{-1} \tag{C4}$$

$$\Omega'^{(2)} = \mathbf{R}_\mathbf{C}\Omega^{(2)}\mathbf{R}_\mathbf{C}^{-1} \tag{C5}$$

To choose some arbitrary components i_1, ..., i_n of $\mathbf{C}'$ and neglect the contribution of other components, the projection matrix $\mathbf{P}$ is defined as

$$P_{ij} = \delta_{ij}(\delta_{ii_1} + ... + \delta_{ii_n}) \quad \text{(C6)}$$

The frequency due to only these components are calculated by substituting $\mathbf{C}'$ with $\mathbf{PC}'$ in eq C3:

$$\omega_{\text{prj}} = \omega^{\text{gas}} + \Omega'^{(1)\dagger}\mathbf{PC}' + \frac{1}{2}\mathbf{C}'^{\dagger}\mathbf{P}^{\dagger}\Omega'^{(2)}\mathbf{PC}' \quad \text{(C7)}$$

Supporting Information Available: The harmonic and anharmonic (third, fourth, fifth, and sixth) force constants of HOD in the gas phase calculated by numerical derivatives of the first analytical derivative of the potential energy at the MP2/6-31+G(d,p) level (Table S1). The dependence of the HOD eigenstate frequencies on n_T (Figure S1). A detailed comparison of the SLE infrared line shape with the cumulant expansion is shown in (Figure S2). This material is available free of charge via the Internet at http://pubs.acs.org.

References and Notes

(1) Ball, P. *Life's Matrix: A Biography of Water*; Farrar, Straus, and Giroux: New York, 1999.
(2) Franks, F., Ed. *Water: A Comprehensive Treatise*; Plenum: New York, 1972.
(3) Eisenberg, D.; Kauzmann, W. *The Structure and Properties of Water*; Oxford University Press: New York, 1969.
(4) Horne, R. A., Ed. *Water and Aqueous Solutions: Structure, Thermodynamics, and Transport Processes*; Wiley: New York, 1972.
(5) Schuster, P., Zundel, G., Sandorfy, C., Eds. *The Hydrogen Bond: Recent Developments in Theory and Experiments*; North-Holland: Amsterdam, 1976; Vol. 1−3.
(6) Wernet, P.; Nordlund, D.; Bergmann, U.; Cavalleri, M.; Odelius, M.; Ogasawara, H.; Naslund, L. A.; Hirsch, T. K.; Ojamae, L.; Glatzel, P.; Pettersson, L. G. M.; Nilsson, A. *Science* **2004**, *304*, 995−999.
(7) Asbury, J. B.; Steinel, T.; Stromberg, C.; Corcelli, S. A.; Lawrence, C. P.; Skinner, J. L.; Fayer, M. D. *J. Phys. Chem. A* **2004**, *108*, 1107−1119.
(8) Wang, Z. H.; Pakoulev, A.; Pang, Y.; Dlott, D. D. *Chem. Phys. Lett.* **2003**, *378*, 281−288.
(9) Laenen, R.; Simeonidis, K.; Laubereau, A. *J. Phys. Chem. B* **2002**, *106*, 408.
(10) Stenger, J.; Madsen, D.; Hamm, P.; Nibbering, E. T. J.; Elsaesser, T. *Phys. Rev. Lett.* **2001**, *87*, 027401.
(11) Stenger, J.; Madsen, D.; Hamm, P.; Nibbering, E. T. J.; Elsaesser, T. *J. Phys. Chem. A* **2002**, *106*, 2341−2350.
(12) Yeremenko, S.; Pshenichnikov, M. S.; Wiersma, D. A. *Chem. Phys. Lett.* **2003**, *369*, 107.
(13) Fecko, C. J.; Eaves, J. D.; Loparo, J. J.; Tokmakoff, A.; Geissler, P. L. *Science* **2003**, *301*, 1698−1702.
(14) Woutersen, S.; Bakker, H. J. *Phys. Rev. Lett.* **1999**, *83*, 2077.
(15) Laenen, R.; Rauscher, C.; Laubereau, A. *Phys. Rev. Lett.* **1998**, *80*, 2622.
(16) Laenen, R.; Rauscher, C.; Laubereau, A. *J. Phys. Chem. B* **1998**, *102*, 9304.
(17) Woutersen, S.; Emmerichs, U.; Bakker, H. J. *Science* **1997**, *278*, 658−660.
(18) Lawrence, C. P.; Skinner, J. L. *Chem. Phys. Lett.* **2003**, *369*, 472−477.
(19) Lawrence, C. P.; Skinner, J. L. *J. Chem. Phys.* **2003**, *118*, 264.
(20) Rey, R.; Møller, K. B.; Hynes, J. T. *J. Phys. Chem. A* **2002**, *106*, 11993.
(21) Rey, R.; Møller, K. B.; Hynes, J. T. *Chem. Rev.* **2004**, *104*, 1915.
(22) Deak, J. C.; Rhea, S. T.; Iwaki, L. K.; Dlott, D. D. *J. Phys. Chem. A* **2000**, *104*, 4866−4875.
(23) Soper, A. K. *Chem. Phys.* **2000**, *258*, 121−137.
(24) Soper, A. K.; Bruni, F.; Ricci, M. A. *J. Chem. Phys.* **1997**, *106*, 247−254.
(25) Fung, B.; Mcgaughy, T. *J. Chem. Phys.* **1976**, *65*, 2970.
(26) Isaacs, E. D.; Shukla, A.; Platzman, P. M.; Hamann, D. R.; Barbiellini, B.; Tulk, C. A. *Phys. Rev. Lett.* **1999**, *82*, 600.
(27) Luzar, A.; Chandler, D. *Nature* **1996**, *379*, 55.
(28) Dellago, C.; Naor, M. M.; Hummer, G. *Phys. Rev. Lett.* **2003**, *90*, 105902.
(29) Chandler, D. *Nature* **2002**, *417*, 491−491.
(30) Geissler, P. L.; Dellago, C.; Chandler, D.; Hutter, J.; Parrinello, M. *Science* **2001**, *291*, 2121−2124.
(31) Asbury, J. B.; Steinel, T.; Stromberg, C.; Gaffney, K. J.; Piletic, I. R.; Goun, A.; Fayer, M. D. *Chem. Phys. Lett.* **2003**, *374*, 362−371.
(32) Bredenbeck, J.; Hamm, P. *J. Chem. Phys.* **2003**, *119*, 1569−1578.
(33) Khalil, M.; Demirdoven, N.; Tokmakoff, A. *J. Phys. Chem. A* **2003**, *107*, 5258−5279.
(34) Krummel, A. T.; Mukherjee, P.; Zanni, M. T. *J. Phys. Chem. B* **2003**, *107*, 9165−9169.
(35) Woutersen, S.; Pfister, R.; Hamm, P.; Mu, Y.; Kosov, D. S.; Stock, G. *J. Chem. Phys.* **2002**, *117*, 6833.
(36) Golonzka, O.; Khalil, M.; Demirdoven, N.; Tokmakoff, A. *Phys. Rev. Lett.* **2001**, *86*, 2154−2157.
(37) Thompson, D. E.; Merchant, K. A.; Fayer, M. D. *J. Chem. Phys.* **2001**, *115*, 317−330.
(38) Woutersen, S.; Hamm, P. *J. Chem. Phys.* **2001**, *115*, 7737.
(39) Woutersen, S.; Hamm, P. *J. Chem. Phys.* **2001**, *114*, 2727.
(40) Zanni, M. T.; Asplund, M. C.; Hochstrasser, R. M. *J. Chem. Phys.* **2001**, *114*, 4579−4590.
(41) Piryatinski, A.; Tretiak, S.; Chernyak, V.; Mukamel, S. *J. Raman Spec.* **2000**, *31*, 125−135.
(42) Merchant, K. A.; Noid, W. G.; Akiyama, R.; Finkelstein, I. J.; Goun, A.; McClain, B. L.; Loring, R. F.; Fayer, M. D. *J. Am. Chem. Soc.* **2003**, *125*, 13804.
(43) Møller, K. B.; Rey, R.; Hynes, J. T. *J. Phys. Chem. A* **2004**, *108*, 1275.
(44) Corcelli, S. A.; Lawrence, C. P.; Skinner, J. L. *J. Chem. Phys.* **2004**, *120*, 8107.
(45) Romero, A. H.; Silvestrelli, P. L.; Parrinello, M. *J. Chem. Phys.* **2001**, *115*, 115.
(46) Woutersen, S.; Bakker, H. J. *Nature* **1999**, *402*, 507.
(47) Allen, M. P.; Tildesley, D. J. *Computer Simulation of Liquids*; Oxford University Press: Oxford, 1987.
(48) Brooks, B. R.; Bruccoleri, R. E.; Olafson, B. D.; States, D. J.; Swaminathan, S.; Karplus, M. *J. Comput. Chem.* **1983**, *4*, 187−217.
(49) Scott, W. R. P.; Hunenberger, P. H.; Tironi, I. G.; Mark, A. E.; Billeter, S. R.; Fennen, J.; Torda, A. E.; Huber, T.; Kruger, P.; van Gunsteren, W. F. *J. Phys. Chem. A* **1999**, *103*, 3596−3607.
(50) Jorgensen, W. L.; Maxwell, D. S.; TiradoRives, J. *J. Am. Chem. Soc.* **1996**, *118*, 11225−11236.
(51) Maaren, P. J. v.; Spoel, D. v. d. *J. Phys. Chem. B* **2001**, *105*, 2618.
(52) Lamoureux, G.; MacKerell, A. D.; Roux, B. *J. Chem. Phys.* **2003**, *119*, 5185−5197.
(53) Yu, H.; Hansson, T.; Gunsteren, W. F. v. *J. Chem. Phys.* **2003**, *118*, 221.
(54) Saint-Martin, H.; Hernández-Cobos, J.; Bernal-Uruchurtu, M. I.; Ortega-Blake, I.; Berendsen, H. J. C. *J. Chem. Phys.* **2000**, *113*, 10899.
(55) Banks, J. L.; Kaminski, G. A.; Zhou, R.; Mainz, D. T.; Berne, B. J.; Friesner, R. *J. Chem. Phys.* **1999**, *110*, 741.
(56) Stern, H. A.; Kaminski, G. A.; Banks, J. L.; Zhou, R.; Berne, B. J.; Friesner, R. *J. Phys. Chem. B* **1999**, *103*, 4730.
(57) Chelli, R.; Procacci, P. *J. Chem. Phys.* **2002**, *117*, 9175.
(58) York, D. M.; Yang, W. *J. Chem. Phys.* **1996**, *104*, 159.
(59) Burnham, C. J.; Xantheas, S. S. *J. Chem. Phys.* **2002**, *116*, 1500.
(60) Xantheas, S. S.; Burnham, C. J.; Harrison, R. J. *J. Chem. Phys.* **2002**, *116*, 1493.
(61) Burnham, C. J.; Xantheas, S. S. *J. Chem. Phys.* **2002**, *116*, 1479.
(62) Burnham, C. J.; Xantheas, S. S. *J. Chem. Phys.* **2002**, *116*, 5115.
(63) Cho, M.; Fleming, G. R. *J. Chem. Phys.* **1994**, *100*, 6672.
(64) Jensen, F. *Introduction to Computational Chemistry*; Wiley & Sons: Chicester, UK, 1999.
(65) Gerber, R. B.; Brauer, B.; Gregurick, S. K.; Chaban, G. M. *PhysChemComm* **2002**, 142−150.
(66) Gerber, R. B.; Chaban, G. M.; Gregurick, S. K.; Brauer, B. *Biopolymers* **2003**, *68*, 370−382.
(67) Lawrence, C. P.; Skinner, J. L. *J. Chem. Phys.* **2002**, *117*, 5827.
(68) Polyansky, O. L.; Jensen, P.; Tennyson, J. *J. Chem. Phys.* **1996**, *105*, 6490.
(69) Lawrence, C. P.; Skinner, J. L. *J. Chem. Phys.* **2002**, *117*, 8847.
(70) Oxtoby, D. W.; Levesque, D.; Weis, J.-J. *J. Chem. Phys.* **1978**, *68*, 5528.
(71) Oxtoby, D. W. *J. Chem. Phys.* **1979**, *70*, 2605.
(72) Oxtoby, D. W. *Adv. Chem. Phys.* **1979**, *40*, 1−48.
(73) Frankland, S. J. V.; Maroncelli, M. *J. Chem. Phys.* **1999**, *110*, 1687−1710.
(74) Rey, R.; Hynes, J. T. *J. Chem. Phys.* **1998**, *108*, 142.
(75) Jorgensen, W. L.; Chandrasekhar, J.; Madura, J. D.; Impey, R. W.; Klein, M. L. *J. Chem. Phys.* **1983**, *79*, 926.
(76) Hayashi, T.; Hamaguchi, H. *Chem. Phys. Lett.* **2000**, *326*, 115−122.
(77) Kwac, K.; Cho, M. H. *J. Chem. Phys.* **2003**, *119*, 2247−2255.
(78) Kwac, K.; Cho, M. H. *J. Chem. Phys.* **2003**, *119*, 2256−2263.

(79) Ham, S.; Kim, J. H.; Lee, H.; Cho, M. H. *J. Chem. Phys.* **2003**, *118*, 3491−3498.
(80) Park, E. S.; Boxer, S. G. *J. Phys. Chem. B* **2002**, *106*, 5800.
(81) Suydam, I. T.; Boxer, S. G. *Biochem.* **2003**, *42*, 12050.
(82) Frisch, M. J., et al. *Gaussian 03, Revision B.05*; Gaussian, Inc: Pittsburgh, PA, 2003.
(83) Kubo, R. In *Fluctuation, Relaxation and Resonance in Magnetic Systems*; ter Haar, D., Ed.; Oliver & Boyd: Edinbourgh, 1962; p 23.
(84) Kubo, R. In *Stochastic Processes in Chemical Physics*; Shuler, K. E., Ed., John Wiley and Sons: New York, 1969; Vol. XV of *Adv. Chem. Phys.*; p 101.
(85) Kubo, R. *J. Math. Phys.* **1963**, *4*, 174.
(86) Jansen, T. l. C.; Zhuang, W.; Mukamel, S. *J. Chem. Phys.* **2004**, *121*, 10577.
(87) Pauling, L. *J. Am. Chem. Soc.* **1935**, *57*, 2680.
(88) Ghanty, T.; Staroverov, V.; Davidson, E. *J. Am. Chem. Soc.* **2000**, *122*, 115.
(89) Hellemans, A. *Science* **1999**, *283*, 5402.
(90) Berendsen, H. J. C.; Grigera, J. R.; Straatsma, T. P. *J. Phys. Chem.* **1987**, *91*, 6269.
(91) Berendsen, H. J. C.; Postma, J. P. M.; Gunsteren, W. F. v.; DiNola, A.; Haak, J. R. *J. Chem. Phys.* **1984**, *81*, 3684.
(92) Berendsen, H. J. C.; van der Spoel, D.; van Drunen, R. *Comput. Phys. Commun.* **1995**, *91*, 43.
(93) van Gunsteren, W. F.; Berendsen, H. J. C. *Mol. Phys.* **1977**, *34*, 1311−1327.
(94) Essmann, U.; Perera, L.; Berkowitz, M. L.; Darden, T.; Lee, H.; Pedersen, L. G. *J. Chem. Phys.* **1995**, *103*, 8577−8593.
(95) Mukamel, S. *Principles of Nonlinear Optical Spectroscopy*; Oxford University Press: New York, 1995.
(96) Hayashi, T.; Mukamel, S. *J. Phys. Chem. A* **2003**, *107*, 9113−9131.
(97) Lehoucq, R. B.; Sorensen, D. C.; Yang, C. *ARPACK Users Guide: Solution of Large Scale Eigenvalue Problems with Implicitly Restarted Arnoldi Methods*; Society for Industrial and Applied Mathematics: Philadelphia, 1998.
(98) Hayashi, T.; Mukamel, S. *Bull. Korean Chem. Soc.* **2003**, *24*, 1097−1101.
(99) Benedicht, W. S.; Gailar, N.; Plyler, E. K. *J. Chem. Phys.* **1956**, *24*, 1139.
(100) Mukamel, S. *Phys. Rev. A* **1983**, *28*, 3480.
(101) Mukamel, S.; Abramavicius, D. *Chem. Rev.* **2004**, *104*, 2073.
(102) Chernyak, V.; Mukamel, S. *J. Chem. Phys.* **2001**, *114*, 10430.
(103) Barsegov, V.; Chernyak, V.; Mukamel, S. *Isr. J. Chem.* **2002**, *42*, 143.
(104) Fogarasi, G.; Pulay, P. *Annu. Rev. Phys. Chem.* **1984**, *35*, 191−213.
(105) Pulay, P. *Mol. Phys.* **1969**, *17*, 197.
(106) Pulay, P. *Mol. Phys.* **1970**, *18*, 473.
(107) Obara, S.; Saika, A. *J. Chem. Phys.* **1988**, *89*, 1540−1559.
(108) Gill, P. M. W.; Pople, J. A. *Int. J. Quantum Chem.* **1991**, *40*, 753−772.